Forcing a three-dimensional, hydrostatic, primitive-equation model for application in the surf zone, Part 2: Application to DUCK94

P.A. Newberger

J.S. Allen

College of Oceanic and Atmospheric Sciences, Oregon State University, Corvallis, Oregon, USA

Abstract. A three-dimensional primitive equation model for application to the nearshore surf zone has been developed. This model, an extension of the Princeton Ocean Model (POM), predicts the wave-averaged circulation forced by breaking waves. All of the features of the original POM are retained in the extended model so that applications can be made to regions where breaking waves, stratification, rotation and wind stress make significant contributions to the flow behavior. In this study we examine the effects of breaking waves and wind stress. The nearshore POM circulation model is embedded within the NearCom community model and is coupled with a wave model. This combined modeling system is applied to the nearshore surf zone off Duck, NC during the DUCK94 field experiment of October 1994. Model results are compared to observations from this experiment and the effects of parameter choices are examined. A process study examining the effects of tidal depth variation on depth-dependent wave-averaged currents is carried out. With identical offshore wave conditions and model parameters, the strength and spatial structure of the undertow and of the alongshore current vary systematically with water depth. Some three-dimensional solutions show the development of shear instabilities of the alongshore current. Inclusion of wave-current interactions makes an appreciable difference in the characteristics of the instability.

1. Introduction

Most previous numerical simulations of the nearshore wave-averaged currents have been obtained using depth-integrated (2D horizontal) models [e.g. *Slinn et al.*, 1998; *Özkan and Kirby*, 1999; *Özkan-Haller and Li*, 2003; *Reniers et al.* 2004] or quasi-three dimensional models [*Van Dongeren et al.*, 1995; *Haas et al.*, 2003; *Zhao et al.*, 2003] forced by gradients of the radiation stress tensor [*Longuet-Higgins and Stewart*, 1964]. In this study we present results from a fully three-dimensional (3D) primitive equation model that has been adapted for use in the nearshore. A 3D model of the wave-averaged circulation in the surf zone provides estimates for time- and depth-dependent alongshore and cross-shore velocity fields. The model includes a direct representation of the effects of turbulent processes for the wave-averaged velocities. It naturally resolves the wave-averaged vertical structure, including the undertow, and thus presumably results in improved estimates of bottom stress. In addition, resolution of the vertical shear of the wave-averaged currents results in explicit representation of the dynamical effects of momentum shear dispersion [*Svendsen and Putrevu*, 1994; *Putrevu and Svendsen*, 1999].

Forcing is calculated from the wave-averaged wave prop-

Paper number .
0148-0227/07/$9.00

erties as described in Part 1 [*Newberger and Allen*, 2007] refered to here as NA1. As discussed in NA1, because of the complexity of surf zone flows, the form of the forcing is derived under the simplifying assumptions of shallow-water waves and depth-independent mean velocities. These assumptions clearly result in over-idealized physics, but they facilitate the rational derivation of wave forcing in a dynamically consistent manner. We use that formulation of the forcing here in an initial attempt to develop and test a 3D modeling capability for the surf zone.

In addition to the wave forcing, the 3D model is capable of including surface stress from the wind and also the effects of stratification and of the rotation of the earth. Consequently, with reasonably straight-forward modification the surf-zone model described here should be appropriate for applications to the combined nearshore and the inner shelf flow fields where all of these factors may be important [*Feddersen et al.*, 1998; *Lentz et al.*, 1999]. In particular for application to the inner shelf, the wave forcing should be derived in a form appropriate for water of arbitrary depth and currents with vertical shear.

The coupled wave and circultaion models are described in Section 2, with details included in the Appendices. The data used for model initialization and for model-data comparisons are described in Section 3. In Section 4, we examine characteristics of two-dimensional (variations with depth and across-shore, uniformity alongshore) solutions, including depth-dependent and depth-averaged momentum balances, for a particular time during the DUCK94 field experiment of October 1994 at Duck, NC. In Section 5, results from a large set of numerical experiments with different parameter values are compared with measurements from a vertical array of current meters mounted on a moveable sled [*Garcez Faria et al.* 1998, 2000]. Particular emphasis is placed on the selection and importance of the surface and bottom roughness lengths. In Section 6, the results of a process study to determine the effects of variations in water depth over a tidal cycle on the spatial structure of currents forced by waves with identical offshore properties are presented. The results of 3D simulations are presented in Section 7. Instabilities of the alongshore current are described for several cases and, in particular, the effects on the characteristics of the instabilities of including wave-current interactions and the vortex force term derived in NA1 are examined.

2. The model

A three-dimensional hydrostatic primitive-equation model has been extended to include wave-averaged forcing by breaking waves. The model is based on the Princeton Ocean Model (POM) [*Blumberg and Mellor*, 1987; *Mellor*, 2004]. The unmodified POM includes forcing by surface stress from wind, surface fluxes of heat and fresh water and bottom stress calculated from a quadratic drag parameterization. A two-equation turbulent closure, the Mellor-Yamada level 2.5 scheme [*Mellor and Yamada*, 1982], is used to calculate turbulent eddy coefficients. In the surf zone additional factors become important. Breaking waves exert a surface stress on the wave-averaged currents and create an increase of near surface turbulence. The onshore flux of mass in the waves must also be taken into account. Interactions of waves and currents near the bottom boundary increase the bottom stress felt by the mean currents above the boundary

layer. These effects must be added to the model to simulate the surf zone currents. A wave model is required to provide the wave-averaged wave energy density, dissipation rate and wavenumber needed to force the wave-averaged circulation. These models are coupled using the NearCom master program [*Shi et al.*, 2005].

2.1. Wave model

The formulation for wave forcing in NA1 requires that the circulation model for the wave-averaged currents be coupled with a wave model that provides wave energy density E, wavenumber vector $\mathbf{k}$ and wave energy dissipation ε_d to the circulation model. With the addition of a wave roller submodel (Appendix A) [*Svendsen*, 1984; *Deigaard*, 1993; *Dally and Brown*, 1995; *Stive and De Vriend*, 1995] the wave roller energy density E_r is also required. The forcing is based on the derivations of NA1 which uses shallow water waves. Here, however, the waves are calculated by a more general linear wave model (Appendix A) so that the wave height and hence the wave dissipation rate can be calculated more accurately. This, in turn, provides a more accurate estimate of the part of the forcing proportional to the surface stress [NA1, *Longuet-Higgins*, 1973] which plays a major role in driving the wave-averaged alongshore current. It is further assumed that the depth-averaged velocities from the circulation model are the appropriate velocities to be used in the wave-current interaction terms in both the wave and the circulation models. The wave model (described in Appendix A) is solved numerically using a finite-difference approximation. It includes evolution equations for the wave action with dissipation, for the wave number components, and for the roller energy density. The surface elevation and the depth-integrated currents from nearshore POM are returned to the wave model with the exchange of data between the two submodels handled by the NearCom master program.

Input to the wave model includes offshore wave height, wave period and direction, wave transformation parameters γ and B [*Thornton and Guza*, 1983, 1986; *Church and Thornton*, 1993] and a roller parameter β [*Nairn et al.*, 1991; *Stive and De Vriend*, 1995]. The data necessary to initialize the wave model are obtained from measurements made as part of the DUCK94 experiment and are discussed in Section 3.

2.2. Wave-averaged circulation model

POM is comprised of evolution equations for the free surface elevation, the horizontal components of the velocity, and the temperature and salinity, which with a non-linear equation of state provide the density. There are also evolution equations for two turbulent quantities q^2, twice the turbulent kinetic energy, and $q^2 l$, which together give the turbulent length scale l. The vertical velocity is calculated from the three-dimensional continuity equation. The momentum equations are modified here (Appendix B) to include the wave-forcing formulation that involves a depth-independent forcing term F_b and an additional surface stress from breaking waves [NA1] (and optionally rollers). Although the wave forcing derived in NA1 is for depth-independent currents and shallow-water waves, we apply it here in a fully 3D circulation model as an approximation. A non-zero velocity perpendicular to the mean surface ($\omega(0)$ in the terrain following σ-coordinates of POM) is required to model the wave-averaged flux of mass from the waves and rollers through

the mean surface [NA1, *Hasselmann*, 1971]. Additionally, the presence of waves modifies the surface boundary conditions for the turbulence quantities and the calculation of bottom stress.

2.2.1. Wave-current bottom boundary layer. The interactions of waves and currents in the bottom boundary layer are important for coastal circulation modeling and particularly so in the nearshore surf zone. [*Feddersen et al.* 1998]. One effect of this interaction is enhanced shear stress felt by the wave-averaged currents above the wave-current bottom boundary layer [e.g. *Grant and Madsen*, 1979]. Two approaches to modeling the effect of the shear stress are included in nearshore POM (Appendix B). The first [*Styles and Glenn*, 2000, 2002] is an extension of the *Grant and Madsen* [1979] bottom boundary layer model (BBLM). This approach calculates the bottom stress felt by the mean currents above the wave-current bottom boundary layer directly from the wave and current properties. This bottom stress then replaces the quadratic drag law stress used in POM. The second approach [*Mellor*, 2002] is to parameterize the effects of wave-current interactions in the bottom boundary layer by modifying the *Mellor-Yamada* [1982] turbulence closure scheme embedded in POM to include additional production of turbulent kinetic energy related to the properties of the waves. With this additional production, bottom stress calculated with the quadratic drag law includes the effects of the wave-current interaction in the bottom boundary layer. We note that some of the effects of sub-grid scale bed forms are not included in this formulation and may be important [*Madsen et al.*, 1991; *Ardhuin et al.*, 2003]. The bottom roughness lengths z_b used in this study are generally consistent with measurements from DUCK94 [*Feddersen et al.*, 2003] and include the effects of small ripples found in the surf zone during this time period.

2.2.2. Wave-enhanced surface turbulence and surface roughness. The surface boundary conditions (Appendix B) for the turbulent quantities q^2 and $q^2 l$ are based on *Craig and Banner* [1994], which requires that a surface roughness length z_s be specified. This quantity is not well known. The nearshore POM implementation includes options for specifying a constant z_s across the surf zone [*Gemmerich and Farmer*, 1999] or for specifying z_s as a fraction of the root mean square wave height [*Burchard*, 2001]. We note that recently *Mellor and Blumberg* [2004] have used an implementation of the *Craig and Banner* [1994] boundary condition with a wave parameterization dependent on wind stress in a simulation of mixing in deep water in the presence of waves. This formulation has not been verified for the surf zone, but is used here to approximate the increased turbulence under breaking waves.

3. Data and initial conditions

For the numerical experiments of Sections 4 and 5, data from the DUCK94 experiment conducted during October 1994 at the U.S. Army Corps of Engineers Field Research Facility (FRF) at Duck, NC are used to initialize the model and for model-data comparisons [*Gallagher et al.*, 1996; *Feddersen et al.*, 1998; *Garcez Faria et al.*, 1998, 2000]. The data are from 12 October 1994 during a storm with winds and waves primarily from the north. At this time, the alongshore topography consists of nearly straight and parallel isobaths [*Garcez Faria et al.* 1998]. There is a well

defined shore-parallel bar located approximately 130 m offshore. The topography is determined from measurements from the Coastal Research Amphibious Buggy (CRAB) and for each model simulation the depth has been adjusted by the tide measured at approximately 8 m depth. The measured topography is smoothed and extended to the offshore limit of the computational domain at 1 km offshore (Figure 1). Both the field measurements and the model results will generally be referenced to a Cartesian coordinate system (x, y, z) with x positive offshore, y positive toward the north and z the vertical coordinate. In most cases, the FRF convention will be used for the direction and origin of the across-shore x coordinate.

Parameters required to initialize the wave model (Table 1) are derived using measurements from the fixed array deployed as part of the DUCK94 experiment and from the array of pressure sensors deployed at the 8 m isobath by the FRF. The wave direction at the 8 m isobath is calculated from the S_{xy} component of the radiation stress tensor [*Elgar et al.*, 1994; *Feddersen et al.* 1998]. This angle is measured counterclockwise from an onshore directed shore normal. A rotation of the coordinate system by 2° clockwise to be aligned more nearly along-isobath has been used in some studies of this time period [e.g. *Garcez Faria et al., 2000*]. The effect of a small rotation of coordinates such as this is felt primarily through the solution sensitivity to offshore wave angle. In this instance the offshore wave angle is increased by 2°. The determinations of the offshore wave height and direction and optimal values of the wave propagation parameters γ and B are made with both the rotated (ISO) along-isobath coordinate system and unrotated (FRF) coordinate system. Both coordinate systems measure offshore distance x from the FRF origin so that the bar is located at approximately $x = 250$ m while the shoreline varies with the tide and is near $x = 119$ m at mid tide. The wave frequency used is the energy-weighted mean of the measured frequencies [*Feddersen et al.*, 1998]. For the time of each model simulation, a best fit γ and B are found by comparing the H_{rms} measured at the 8 m isobath and at the fixed array locations to that obtained from the wave action equation without wave-current interaction using the *Thornton and Whitford* [1990] wave energy dissipation formulation [*Church and Thornton*, 1993] (Appendix A) and assuming alongshore uniformity and time independence. The roller parameter β is taken to be 0.1 in all cases. The best fit values of γ and B are then used to determine the wave height H_{rms} and direction θ at the offshore boundary of the computational domain located 1 km from the coastline. The values of γ and B obtained are consistent with previous estimates and do not vary greatly from one solution to another (Table 1). A comparison between the wave height predicted by the wave model and the observations from the fixed array is shown in Figure 1. Additional forcing by wind stress calculated from winds measured on the FRF pier [*Feddersen et al.*, 1998] is used in some of the simulations.

Measurements utilized for model-data comparison include vertical profiles of velocity measured from a stack of 7 current meters mounted 42, 68, 101, 147, 179, 224 and 257 cm above the bottom on a moveable sled [*Garcez Faria et al.*, 1998, 2000]. The sled was towed to a location outside the bar, data were recorded for approximately one hour, and the sled was then pulled to a position nearer the shore. Each hour-long period of measurements is referred to as a num-

bered sled run (Table 1). Measurements were made from early morning to evening, spanning the high tide period of 12 October and were averaged over the period of each run. Data were recorded at 7 locations on 12 October 1994 from about 46 m outside the bar through the trough. The data from the sled are originally in the ISO coordinate system. For comparison with the model runs in the FRF coordinates these data are are rotated into the FRF orientation. In addition, more limited model-data comparisons are made utilizing the fixed array velocity measurements [*Gallagher et al.*, 1996; *Feddersen et al.*, 1998]. The process studies of Sections 6 and 7 use topography from 12 October 1994.

4. Characteristics of model solutions

The experiments of this section are run in two-dimensional (2D) mode with spatial variations in depth z and offshore x and uniformity assumed alongshore y. The horizontal resolution is 4 m and there are 30 σ-levels in the vertical. The experiments assume steady offshore wave conditions and the solutions are run to a steady state. The σ-levels are distributed so that there is relatively high resolution near the surface and bottom. In the following we use the designation experiment to refer to a particular choice of parameters or coordinate system (Table 2). In Sections 4 and 5, each experiment includes a set of model simulations obtained for different times, corresponding to particular sled runs, and thus for different tide heights and offshore wave conditions. Except as noted in Table 2, the measured wind stress (Table 1) is included in the forcing.

The output of nearshore POM includes full 3D fields of velocities, the turbulence quantities q^2 and $q^2 l$ as well as optional time series and the terms in both depth-averaged and depth-dependent momentum balances (Appendix B). The results from a simulation for the conditions of sled run 4 (one of the 7 model runs comprising Experiment 11 of Table 2) are shown in Figures 2-4. The conclusions of the model-data comparisons in Section 5 show that the inclusion of rollers is typically necessary to obtain the best agreement. Consequently, this simulation includes rollers. Forcing by wind stress is also included. The across-shore velocity fields (Figure 2) are characterized by onshore flow near the surface, strongest near the bar location, and a strong offshore undertow beneath. In the two-dimensional (alongshore uniform) simulations, the depth-integrated model across-shore flow in the surf zone is typically nonzero and positive since it must locally balance the onshore flow associated with the time-averaged Eulerian wave mass flux and the surface mass flux of the rollers. The offshore transport in the undertow is balanced by both onshore flow associated with the waves and by the onshore flow near the surface in the mean circulation forced by the surface stress. The alongshore jet is centered in the trough and is strongest at the surface. Intense mixing is located in the regions of wave breaking over the bar and at the shore, with relatively large values of the turbulent kinetic energy ($q^2/2$) and eddy coefficients (K_M) extending into the water column from the surface.

The primary balance in the depth-dependent across-shore x momentum equation (Figure 3) (see Appendix B for description of the momentum balance terms) is between vertical diffusion that is approximately depth-independent and the across-shore pressure gradient representing the wave set up. The body force, consisting of the vortex force related

term and a term arising from the radiation stress gradient (NA1), and the advection term are smaller but not negligible. The balance in the alongshore y momentum equation is primarily between advection and vertical diffusion. Both of these terms show substantial depth-dependence with the advection term over the bar having relatively large magnitudes, negative near the surface where $u < 0$ and positive in the bottom part of the water column where $u > 0$. This behavior clearly reflects the effect of advection of alongshore momentum v, where at this location $v_x > 0$, by the across-shore velocity u. The vertical diffusion term generally balances the advection over the bar. The body force, which in the alongshore uniform case here consists only of the vortex force term, is smaller but not negligible over the bar.

Depth-averaged currents (U, V) for Experiment 11 (Figure 4, left panel) show a strong alongshore jet in V, with largest magnitudes in the outer part of the trough, and a non-zero across-shore velocity U, where the transport DU balances the onshore flux by the waves and rollers. The set up, evident in the plot of surface elevation η, shows large gradients at the locations of wave breaking over the bar and at the coast. The depth-averaged across-shore x momentum equation (Figure 4, left panel) shows a balance between the forcing, including both the surface stress and the body force, and the pressure gradient. The body force is primarily due to the radiation stress gradient given by the first term in (B7). Bottom stress and advection make only small contributions. The depth-averaged alongshore balance is between the positive forcing and negative bottom stress, with a significant positive contribution from the advection offshore of $x = 100$ m. The surface stress is large and positive over the bar while the body force acts to reduce the total force over the bar and to increase the force within the trough. In the two-dimensional case of alongshore uniformity, the body force in the y-momentum equation is equal to the vortex force term, the second term in (B8).

To allow an assessment of the effect of rollers, results from Experiment 16, which is identical to Experiment 11 but with rollers omitted, are shown in Figures 4-6. The major qualitative difference is in the structure of the alongshore velocity which, without rollers (Figure 5) has the largest magnitude velocity confined in a much narrower region in the vicinity of the bar. The alongshore velocities in the trough are relatively weak (Figure 5) increasing in magnitude in a narrow nearshore region and with large gradients in the outer part of trough bordering the strong jet-like alongshore flow over the bar. Across-shore velocities u are generally larger in magnitude without rollers (Figure 5) and with the location of the region of strongest flow, both near the surface and in the undertow, displaced to the offshore side of the bar. The stronger across-shore velocities u, combined with the increased horizontal shear in v, lead to larger contributions in the alongshore momentum balance of the advection term (Figures 4, 6). Vertical diffusion in the alongshore balance is correspondingly also of larger magnitude in the region of strong advective effects (Figure 6), with larger values of the turbulent kinetic energy and the eddy coefficient K_M found at greater depth in this region (Figure 5). Evidently, as a result of the relatively large values of V_x just inshore of the bar, the contribution of the vortex force term to the alongshore momentum balance is appreciable in that region (Figure 6). The depth-averaged alongshore momentum balance in Figure 4 (right panel), shows that near and offshore

of the bar the positive surface stress term is dominant, but the net force is reduced by a negative vortex force. Inshore, however, the forcing is nearly entirely from a positive vortex force. Without the rollers, both components of the forcing are small in the inner trough. In the across-shore momentum balance (Figures 4, 6) the advective effects are considerably larger without rollers, presumably related to larger positive values of uu_x near the surface over the bar.

Overall, the most significant effects of the roller model is to increase the forcing in the alongshore momentum balance in the trough relative to that over the bar (Figure 4), and thus to qualitively alter the structure of the alongshore currents as described above. The model-data comparisons in Section 5 will show that this alteration, with stronger alongshore currents in the trough, leads to better agreement between model studies and observations.

Two experiments, 18 and 19 in Table 2, are run to assess the effects of the wave-current interactions. In both experiments, the vortex terms (B7) and (B8) are omitted from the mean momentum equations (B3) and (B4) and the depth-averaged velocities are omitted from the wave model (A1) and (A7). Figure 7 shows the depth-averaged velocities, surface elevation and momentum balances for Sled Run 4 of experiment 18 which includes rollers and experiment 19 which does not. In both cases, the depth-averaged across-shore balances and velocity are essentially unchanged from experiments 11 and 16 respectively. This indicates, as noted previously in connection with Figure 4, that the body force in the across-shore direction is primarily from the contribution of the radiation stress gradient [NA1; *Longuet-Higgins*, 1973; *Smith*, 2006]. The situation is different in the alongshore momentum balance where, in the alongshore uniform simulations here, the body force consists only of the vortex force term. Comparison of experiment pairs, 11 and 18, and 16 and 19 shows that with or without rollers, the vortex force acts to reduce the magnitude of the total positive alongshore forcing over, and offshore of, the bar and to increase the forcing onshore of the bar in the outer part of the trough. Consequently, with and without rollers, the inclusion of the vortex force acts to reduce the magnitude of the alongshore current over the bar and to displace the location of the maximum velocity onshore.

5. Model-data comparisons

The numerical experiments run to assess different parameter choices through model-data comparisons are listed in Table 2. Each experiment consists of 7 model simulations, one for the conditions during each sled run on 12 October 1994. For each of the 7 simulations, model output is interpolated to the location of the measurements (one vertical profile per simulation). Vertical profiles of across-shore velocity u and alongshore velocity v from Experiment 11 are shown in Figure 8 (top) together with the corresponding sled data. This experiment is in the ISO coordinate system, uses the *Styles and Glenn* [2000, 2002] bottom boundary layer model (BBLM) and relatively small bottom roughness $z_b = 0.001$m. This corresponds to a physical roughness of 0.03 m consistent with measurements from DUCK94 [*Feddерson et al.*, 2003]. Each model profile is from a separate simulation corresponding to the time period of the measurements. In general, we find very good agreement between the alongshore velocities in the model and the data. The agree-

ment is somewhat less good for the across-shore velocities, especially directly over the bar. We note that, as discussed below, the agreement between model and data is essentially similar (Figure 8 (bottom)) in the case of Experiment 1 (Table 2) where the FRF coordinate system is used, resulting in a smaller offshore wave angle, and where the Mellor bottom boundary layer parameterization (BBLP), which generally results in a smaller bottom stress than the *Styles and Glenn* [2000, 2002] BBLM, together with a larger bottom roughness length of $z_b = 0.005$ m are used as required for good agreement. Other combinations of BBLM or BBLP, roughness lengths and coordinate orientation with compensating effects would likely lead to similar results as well.

The data-model error is calculated for each profile as

$$\Xi_j = \left\{ \frac{\sum_{i=1}^{nsen(j)} (d_{ij} - m_{ij})^2}{\sum_{i=1}^{nsen(j)} d_{ij}^2} \right\}^{\frac{1}{2}} , \qquad (1)$$

where j is the sled run number, i the sensor number, $nsen(j)$ is the number of sensors [*Garcez Faria et al.*, 2000] used in that profile and d_{ij} and m_{ij} are the sled data and model output values at the (i, j) location, respectively. The composite error $\tilde{\Xi}$ is the mean of Ξ_j taken over the 7 sled stations for each experiment. Errors are calculated for the u and v components of the velocity separately.

Figure 9 shows the composite errors $\tilde{\Xi}$ for the 19 experiments. The experiments 1-11 in the top panel are those with variations in roughness lengths z_s and z_b, choice of bottom boundary layer model and of coordinate system orientation (FRF or ISO). The experiments 1 and 11 (Figure 8) are marked with filled squares.

We examine the sensitivity of the errors to the choice of both the surface and bottom roughness lengths using the *Mellor* [2002] BBLP. The experiments 1-4 differ only in the choice of surface roughness length z_s. The composite errors for the alongshore velocities v are almost independent of the choice of z_s, while the errors for u vary, with the smallest values for the largest z_s (Experiment 3). Figure 10 shows vertical profiles of u from Experiments 1-4 for the sled runs 4 and 6. We see that the primary effect of larger surface roughness is to reduce the vertical gradient in the across-shore velocity. This change in shape results in poorer agreement in the outer part of the trough (run 4) and improved agreement in the inner part of the trough (run 6) and also offshore of the bar (not shown) where the vertical gradients in the measured currents are small. For Experiments 2 and 4, the changes in shape of the u profiles occur mostly above the level of the measurements and have little effect on the error estimates. The alongshore velocities v have relatively small vertical gradients in the middle of the water column and thus the errors are less sensitive to changes in surface roughness.

Varying the bottom roughness (Experiments 1, 5 and 6) has little effect (Figure 9) on the errors in u as expected from the small relative value of the bottom stress term in the depth-averaged across-shore momentum balances in Section 4. For these experiments, the largest composite error in the alongshore velocity v occurs at the smallest value $z_b = 0.001$ (Experiment 5) where the model consistently over estimates the alongshore flow.

Comparison of Experiments 1 and 7, using the *Mellor* [2002] BBLP, and Experiments 10 and 11, using *Styles and*

Glenn [2000, 2002] BBLM shows the sensitivity of the model results to a small change (2°) in the offshore wave angle. The differences in the measured currents in the two coordinate systems (Figure 8) are barely distinguishable by eye. The change in forcing, however, makes a significant difference in the model results. For example, for run 4, Experiments 10 and 11, Figure 11 shows an increase in the depth-averaged alongshore current of about 0.1 ms^{-1} corresponding to the small change in coordinate system.

Experiments 8, 9 and 10 show the effect of choice of z_s and z_b when using the *Styles and Glenn* [2000, 2002] BBLM. The largest composite error in the alongshore velocities (Figure 9) is found in Experiment 8, which differs from Experiment 1 only in the choice of bottom boundary layer formulation. Evidently, with the same bottom roughness length, the effects of waves on the bottom stress is greater for the *Styles and Glenn* [2000, 2002] BBLM, as the alongshore current magnitudes from the model are consistently smaller than those in the data. Decreasing the bottom roughness length to $z_b = 0.001$ m (Experiment 9, 10 and 11) improves the agreement with data to levels comparable with the *Mellor* [2002] BBLP experiments (3, 1 and 7). Modification of the surface roughness (Experiments 9 and 10) gives results consistent with those shown in Figure 10.

The bottom panel of Figure 9 includes the results of Experiments 12-14 and 15-19 in which the forcing by rollers and/or wind is omitted from Experiment 1 and 11. Results from Experiments 1, 11, 7 and 10 are repeated for comparison. We see that the effect of omitting only the wind (Experiments 12, 15), which in this case acts to increase the alongshore current, is relatively small as expected in the surf zone. The errors increase without the roller model (Experiments 13, 14, 16, 17). As discussed in Section 4, the roller is important in both the alongshore velocity, where the alongshore current is greatly reduced in the trough without the roller, and the across-shore velocity, where the effect of omitting the roller is to shift the location of the undertow offshore (Figures 2, 5). Omission of both wind and roller (Experiments 14, 17) increases the error in both u and v over that for the corresponding no roller experiments (13, 16). As measured by the composite error, the effect of omitting the roller is comparable to that of changing the coordinate system orientation although the differences in the profiles leading to the errors are very different. Finally, a comparison of the results for the experiment pairs (11, 18) and (16, 19) (Figure 9) shows similar errors in u, but a noticeable increase in the errors in v when the vortex force terms in the momentum equations and the wave-current interaction terms in the wave model are omitted.

An additional model-data comparison, that allows some assessment of model solution spatial variability at a fixed time, is made with hourly average velocity data from the fixed array. The fixed array extends farther offshore than the sled measurements but there is only one current meter at many locations. Velocities from Experiments 11 and 16, sled run 4, whose solution characteristics are discussed in Section 4, are compared with the fixed array data averaged over the hour beginning at 1200 (Figure 12). For Experiment 11 the agreement is good in the trough for both u and v. Offshore of the bar the model undertow is larger than that in the measurements, while the model alongshore currents are weaker and more vertically sheared than the data. Results from Experiment 16 (Figure 12 bottom) show that the roller

is not important offshore of the bar. The model alongshore velocities without the roller are notably weaker than the measurements in the trough as are the model velocities in the undertow.

The model, with properly chosen parameters, gives good agreement with field data from the DUCK94 experiment. Including the roller in the formulation is necessary to obtain the best agreement. The model results are sensitive to the choice of parameters such as surface and bottom roughness, to orientation of the coordinate system (as reflected in the value of the offshore wave angle), to the method of parameterization of the wave-current effects in the wave bottom boundary layer and to the inclusion of the vortex force in the momentum equations and the wave-current interaction terms in the wave model.

6. Tidal effects on wave-forced currents

Thornton and Kim [1993] have examined data from the DELILAH field experiment conducted at Duck, NC in October 1990 to determine the modulation of wave heights and alongshore currents at tidal frequencies. They find that wave heights and alongshore currents inside the surf zone show a strong tidal signature. They show further that the changes in depth due to the tides are a dominant cause of this variability.

We apply the nearshore model to three alongshore uniform cases where the only differences between the simulations are variations in the water depths due to tides. The three cases use the bottom topography from 12 October 1994 with the depth adjusted to the measured high, mid and low tide conditions for that day. The offshore wave height 1.5 m, wave period 6 s, and direction 9° are typical of that day. The model runs use $\gamma = 0.32$, $B = 0.65$ with the *Thornton and Whitford* [1990] dissipation formulation [*Church and Thornton*, 1993]. The surface roughness z_s=0.3 m, bottom roughness z_b=0.001 m and the *Styles and Glenn* [2000, 2002] bottom boundary layer model are used. There is no wind forcing. The horizontal resolution is 2 m and there are 30 σ levels. These parameter choices are similar to those of Experiment 15 (Table 2) with values typical of 12 October 1994 for γ and B and the offshore wave properties.

Figure 13 shows the topography and calculated wave heights with the across-shore x axis measured in the FRF coordinates so that the bar position remains fixed at $x \approx 253$ m and the shoreline moves with depth changes. The waves at low tide begin breaking farther offshore and are reduced in amplitude over the bar and in the trough relative to the other time periods. At high tide, the decrease in wave height as the waves propagate toward shore is restricted to the region near the bar. The depth-averaged alongshore velocities in Figure 14 show that the current maximum is shifted onshore with increasing water depth. The maximum depth-averaged alongshore current occurs at mid tide. Alongshore velocities in the inner part of the trough are large at high tide while velocities in the outer part of the trough and over the bar increase at low tide. Figures 13 and 14 agree qualitatively with Figure 11 of *Thornton and Kim* [1993] based on data from the DELILAH field experiment taken under conditions similar to those of 12 October 1994 with a well formed bar and moderate waves. In particular, the phase relationship between the tidal height and the alongshore velocities in the inner part of the trough and over the bar found

in the data is reproduced here.

Profiles of horizontal velocities u and v (Figure 15) at the locations of the sled measurements show the depth variation of the velocities for the high and low tide cases. For both high and low tide, the undertow is strong over the bar and on the outer flank. At high tide, large offshore velocities are found in the outer part of the trough as well. In both cases, the near-surface flow is directed onshore with magnitude close to that of the undertow velocities.

Table 3 summarizes the changes in the flow with tidal height. The maximum offshore velocity over the bar u_{bar} is greatest for high tide conditions. The offshore transport over the bar T_{bar} increases with water depth more rapidly than the maximum offshore velocity over the bar u_{bar} as tide height increases. The maximum offshore velocity u_{max} is located just outside the bar and moves to a location farther offshore as the tidal height decreases. The maximum magnitude of the alongshore velocity is found at mid tide in agreement with the observations in *Thornton and Kim* [1993]. The location of the maximum alongshore velocity shifts into the trough as the tidal height increases and is approximately 40 m inside the bar near the center of the trough at high tide.

7. Three-dimensional experiments and instabilities

Both observations [e.g. *Oltman-Shay et al.* 1989; *Reniers et al.*, 1997; *Noyes et al.*, 2004] and previous modeling studies [e.g. *Allen et al.*, 1996; *Reniers and Battjes*, 1997; *Slinn et al.*, 1998; *Özkan and Kirby*, 1999] have shown that an alongshore current forced by breaking surface gravity waves may be unstable, exhibiting shear instability disturbances with wavelengths of O(100 m) and periods O(100 s). Linear stablility analysis of the depth-integrated equations [e.g. *Reniers et al.*, 1997; *Noyes et al.*, 2004] have shown that unstable modes associated with typical alongshore currents have characteristics consistent with observations.

Results from a linear stability analysis applied to the 3D primitive-equation model are not presently available. Consequently, the wavelengths of possible unstable disturbances are not known apriori and must be determined from nonlinear 3D experiments. We run numerical experiments with the nearshore POM model in an alongshore periodic channel of length 500 m with 4 m horizontal resolution and 30 σ-levels to examine possible instabilities of the currents. The topography is alongshore uniform in all cases and the experiments are initialized with the steady two-dimensional solutions for the same parameter set. A small spatial perturbation is applied to the surface forcing for the first 0.2 h of the each experiment. After that time, the forcing is not perturbed, but may not be alongshore uniform because of wave-current interaction terms in both the wave equations and the forcing terms. In all of the 3D experiments discussed here the instabilities that develop essentially equilibrate as time increases, i.e., they result in disturbances of nearly uniform, or weakly pulsating, form propagating alongshore. All the results presented, where instabilities develop, are for this equilibrated state.

In these experiments, the *Thornton and Guza* [1983, 1986] wave dissipation is used in the wave model with $\gamma = 0.3$ and $B = 0.65$. The offshore wave height is 1.6 m with 10 s period. Eight 3D experiments with parameters described and

numbered in Table 4 are used in this analysis. The bottom roughness for all runs is $z_b = 0.001$ m and the wind stress corresponding to the time period of sled run 4 is included in the forcing. None of these experiments include rollers and, in fact, all of the experiments that were tried with rollers were found to be stable. This result appears to be at odds with observations, since instabilities of the alongshore current are found in situations where rollers are surely present. A possible explanation may be that the forcing in nature is not steady, but varies on several time scales including that of the wave groups, and that this time-dependence may contribute to forcing the finite amplitude development of modes that are otherwise marginally stable. Another possibility is that the length of the periodic domain is insufficient for instabilities to grow, but based on estimates of wavelengths of observed instabilities [e.g., *Oltman-Shay et al.*, 1989; *Noyes et al.*, 2004] that seems less likely. Modeling factors such as too much dissipation from bottom friction, or inadequacies in either the forcing formulation or in the submodel for the rollers may also contribute to the stability of the alongshore current in the numerical experiments.

Figure 16 shows u and v horizontal fields at σ-level 2 near the surface for experiments 1-4 (Table 4). The impact of including both wave-current interactions in the wave model and including the vortex force related term in the forcing of the mean currents is illustrated by the differences in the results. In all runs, the instabilities are relatively regular, similar to the results from shallow-water (SW) experiments with intermediate bottom friction values, but unlike the more irregular and turbulent regimes found in the SW models with lower values of bottom friction [*Allen et al.*, 1996; *Slinn et al.*, 1998; *Özkan and Kirby*, 1999]. In agreement with other results from SW simulations [*Özkan-Haller and Li*, 2003], the inclusion of wave-current interactions decreases the strength of the instabilities. The two experiments with the vortex force term omitted from the forcing show different character from the complete model. With wave-current interaction and no vortex force the solution does not show instability, while without wave-current interaction the instabilities have different structure and wavelength.

Across-shore sections of velocity from Experiment 1, with wave-current interaction and vortex force included, are shown in Figure 17. We denote the alongshore average by brackets $< >$ and deviations about the average by primes so that, for example,

$$u = < u > + u', \qquad < u' > = 0. \tag{2}$$

The top row shows the alongshore average $< u >$ and $< v >$. For comparison, the second row shows u and v from a corresponding 2D experiment. The alongshore-averaged jet is broader, with smaller maximum speed than that in the 2D experiment. The alongshore-averaged field of across-shore velocity $< u >$, however, is seen to be virtually identical to that from the 2D case. The third and fourth rows are sections at two y locations of u' and v', (see Figure 16 for location). The perturbations show little vertical structure and are located primarily between the bar crest and the shore.

Changes in parameters and topography modify the three-dimensional flow. Figure 18 shows the u and v fields near the surface for Experiments 5-8 (Table 4). In Experiments 5 and 6, with modified surface roughness, $z_s = 0.2$ m and

$z_s = 0.3 \times H_{rms}$, respectively, the perturbations and jet structure are modified, but show the same qualitative features as discussed above. With the low tide topography (Experiment 7) the perturbations again fill the trough although the mean alongshore velocities in the trough are much smaller. The magnitudes of the perturbation velocities (not shown) are greater than in the deeper case. With reduced offshore wave angle (Experiment 8) the magnitude of the alongshore jet is reduced and, correspondingly, so is the magnitude of the perturbations.

The differences in the 3D solutions shown in Figure 16 give an indication that utilization of a wave forcing formulation that includes wave-current interactions and the vortex force term may influence the characteristics of the response. An additional point to note is that the instabilities found are relatively weak and typically not overly energetic. Moreover, when rollers are included the flows are generally stable. Since the 3D model does not have readily identified parameters that can be adjusted within reasonable limits to appreciably reduce dissipative effects, it appears that the resolved momentum shear dispersion mechanism [*Svendsen and Putrevu*, 1994; *Putrevu and Svendsen*, 1999; see discussion in Section 8] may contribute to stabilizing the alongshore current. Similar qualitative findings are reported by *Zhao et al.* [2003] based on numerical experiments with a quasi-three-dimensional model. These results raise a question about the possible importance of time variations in the wave field in forcing observed instabilities of alongshore currents.

8. Discussion

The modeling results for the wave-averaged circulation in the nearshore surf zone during the DUCK94 field experiment obtained here with an appropriately modified three-dimensional primitive-equation model offer strong encouragement for the potential benefits from the use of such an approach. The encouragement comes, in particular, from the generally favorable comparisons found between the sled velocity measurements and the depth-dependent model velocities. The accuracy of the model solutions depends on the choice of parameterizations, e.g., that for the effects of the wave-current bottom boundary layer and, clearly, that for the turbulence itself, whose applicability to observed surf zone flows has not been tested. In addition, given the choice of parameterizations used here, there exist a number of important parameters, e.g. the surface and bottom roughness lengths, whose optimum specification for surf zone flow remains uncertain. The sensitivity found in the model velocity fields to the offshore wave angle, and thus more generally to the wave model and its implementation, likewise may be a cause for concern. Additional experience with applications of this type of model to observed surf zone flows should lead to improved parameterizations and to increased knowledge concerning choices of parameter values.

A comparison of the results obtained with different formulations for the forcing in the 2D experiment pairs (11,18) and (16, 19) (Figure 9) shows that omission of the vortex force term in the momentum equations and the wave-current interaction terms in the wave model leads to an increase in the composite errors in v. The results of the 3D experiments (Figure 16) also show a sensitivity of the solutions to the same difference in the forcing. Consequently, both the 2D and the 3D comparisons indicate that the inclusion of

the vortex force terms and of the wave-current interactions in the wave model may be important for modeling wave-averaged circulation in the surf zone. This conclusion has to be qualified by the limitation that, although the model velocities vary in the vertical, depth-averaged velocities are used to calculate those terms following the results of the idealized analysis in NA1. In the 2D experiments, however, the vortex force depends on the across-shore derivative of the depth-averaged alongshore velocity V_x. Since the depth-averaged V is not an unreasonable representation for $v(z)$ over most of the water column (Figure 8), the use of the depth-averaged currents seems likely to give an acceptable approximation for the vortex force in those experiments. In any case, further theoretical studies that properly account for the effects of vertical shear in wave-averaged surf zone currents are needed. Those studies should provide modified formulations for the wave forcing that may be important for nearshore modeling applications.

The rather strong dependence of the model solutions on the use of a roller submodel, because of the rather uncertain approximate nature of these submodels, is a definite weakness at least for beaches with an offshore sand bar, such as found during DUCK94. That weakness, however, seems at present to be shared by most wave-averaged models and is indicated specifically by the data assimilation study of *Feddersen, et al.* [2004]. We find that the rollers are necessary for the best agreement with the data in the 2D vertical simulations while they act to supress the shear waves in the 3D process studies. Improvements in model representation of the complicated turbulent processes associated with surface rollers would be of obvious value. Linear stability analyses of the 3D equations with and without rollers is also needed to provide insight into the generation of shear waves.

On the positive side, the model is capable of providing time-dependent predictions for three-dimensional spatial variations in the wave-averaged, depth-dependent alongshore and across-shore velocity fields. Information of that type has not been convincingly obtained from other modeling approaches. Moveover, as argued by *Svendsen and Putrevu* [1994], vertical shear in the wave-forced currents can lead to momentum dispersion that acts as an additional mechanism to modify depth-dependent currents. The model applied here explicitly resolves the depth-dependent effects leading to this dispersion. The presence of the dynamical processes involved with the momentum shear dispersion mechanism is indicated by the importance of the advective term in the depth-integrated alongshore momentum balances (Figure 4) and by the strong depth variations of the advective term in the corresponding depth-dependent alongshore momentum balances (Figures 3 and 6). It seems clear that the present modeling approach provides an effective method to properly resolve these effects.

Finally, we note again that a substantial potential advantage of the present approach is that it provides a capability to simultaneously model flow on the inner shelf, where wind and buoyancy forcing along with the effects of density stratification and the earth's rotation can be important, and flow in the surf zone, where wave forcing dominates, and to model possible interactions between these two different flow regimes. Additional work is required to extend the derivation of the wave forcing to nonlinear, or weakly nonlinear, waves that are not restricted to shallow water and to depth-dependent mean currents. We have presented here an initial

framework that should be modified for more general cases as warranted by further research.

Appendix A: The wave model

We follow closely the formulation of *Özkan and Kirby* [1999] with the simplifications that here the shoreline is fixed and all derivatives are calculated using finite difference methods. The energy density equation is replaced by the wave action equation. The equations for the waves in arbitrary depth water are used in the wave model. As discussed in NA1, the waves are assumed to be linear in the derivation of the forcing. Furthermore, shallow-water dynamics is assumed to apply to both the waves and the currents to facilitate derivation of dynamically-based approximate forcing in the surf zone. In the applications here we have chosen to use a linear wave model formulated for arbitrary water depth to estimate the wave- and depth-averaged wave properties required to calculate the forcing. The rationale for this choice is that such a model will give better agreement with the observed wave field than will a shallow-water model. Additionally, the empirical wave dissipation formula [*Thornton and Guza*, 1983, 1986] is determined using arbitrary depth waves. Thus the wave dissipation rate estimate, which is important in driving the alongshore current (B13), will be more accurate and should improve model-data agreement.

The wave action equation including dissipation by breaking waves is given by

$$\frac{\partial}{\partial t}\left(\frac{E}{\omega_r}\right)+\frac{\partial}{\partial x}\left\{\left(c_g^x+U\right)\frac{E}{\omega_r}\right\}+\frac{\partial}{\partial y}\left\{\left(c_g^y+V\right)\frac{E}{\omega_r}\right\} = -\frac{\varepsilon_d}{\omega_r}, \tag{A1}$$

where $E=gH_{rms}^2/8$ is the wave energy density divided by the constant water density, H_{rms} the root mean square wave height, g the gravitational acceleration, ω_r is the relative frequency, (c_g^x,c_g^y) are the (x,y) components of the wave group velocity vector. The velocities $U(x,y,t)$ and $V(x,y,t)$ are depth-averaged velocities from the circulation model (Appendix B) and may be set to zero in the wave subprogram for cases where wave-current interactions are neglected. The wave dissipation ε_d is calculated from the *Thornton and Guza* [1983, 1986] formula,

$$\varepsilon_d=\frac{3\sqrt{\pi}}{16}g\frac{B^3f_p}{\gamma^4D^5}H_{rms}^7, \tag{A2}$$

or from the modification of this formula by *Thornton and Whitford* [1990] as described in *Church and Thornton* [1993],

$$\varepsilon_d=\frac{3\sqrt{\pi}}{16}g\frac{B^3f_p}{D}H_{rms}^3\left[1+\tanh\left(8\left(\frac{H_{rms}}{\gamma D}-1\right)\right)\right] \times\left[1-\left(1+\left(\frac{H_{rms}}{\gamma D}\right)^2\right)^{-\frac{5}{2}}\right], \tag{A3}$$

where D is the water depth, B and γ are empirical constants, $f_p=T_p^{-1}$ is the peak frequency of the waves. The wave spectrum is thus assumed to have a narrow peak in frequency so that it can be approximated by a single frequency.

The other equations in the wave model are for the evolution of the wavenumber vector $\mathbf{k}$ [*Özkan-Haller and Li*,

926 2003],

$$\frac{\partial k^x}{\partial t} + \frac{\partial \omega}{\partial x} = 0, \quad \frac{\partial k^y}{\partial t} + \frac{\partial \omega}{\partial y} = 0, \tag{A4}$$

928 where $\mathbf{k} = (k^x, k^y)$. The absolute frequency ω is found from
929 the dispersion relation

$$(\omega - k^x U - k^y V)^2 = gK \tanh(KD) \equiv \omega_r^2, \tag{A5}$$

931 where K is the magnitude of $\mathbf{k}$. The components of the wave
932 mass flux are given by

$$M_w^x = \frac{E \cos\theta}{c}, \quad M_x^y = \frac{E \sin\theta}{c}, \tag{A6}$$

934 where θ is the direction of the wave propagation in the model
935 coordinate system.

936 We also allow for the inclusion of surface rollers [*Svend-*
937 *sen*, 1984; *Nairn et al.*, 1991; *Deigaard*, 1993; *Stive and De*
938 *Vriend*, 1995] primarily following the formulation in *Reniers*
939 *et al.*, [2004] (see also *Reniers et al.* [2002]). The roller
940 energy density E_r is calculated from the equation

$$\frac{\partial E_r}{\partial t} + \frac{\partial}{\partial x}\left\{2\left(c^x + U\right)E_r\right\} + \frac{\partial}{\partial y}\left\{2\left(c^y + V\right)E_r\right\} = \varepsilon_d - \varepsilon_r, \tag{A7}$$

943 with ε_r calculated as

$$\varepsilon_r = \frac{g \sin\beta E_r}{c}, \tag{A8}$$

945 [*Stive and De Vriend*, 1995]. Again the influence of the
946 depth-averaged mean currents U and V may be omitted
947 from these equations if wave-current interactions are ne-
948 glected. The gradients of the roller radiation stress are as-
949 sumed to act at the mean surface (B14) with the radiation
950 stress given by

$$S_{xxr} = 2E_r \cos^2\theta, \quad S_{xyr} = 2E_r \sin\theta\cos\theta, \quad S_{yyr} = 2E_r \sin^2\theta. \tag{A9}$$

953 The mass flux in the rollers [*Svendsen*, 1984] has components

$$M_r^x = \left(2E_r \cos\theta\right)/c, \quad M_r^y = \left(2E_r \sin\theta\right)/c, \tag{A10}$$

955 where M_r and E_r are divided by the constant density as
956 above. The divergence of this flux contributes to the mean
957 surface normal velocity $\omega(\sigma = 0)$ in the σ-coordinate system
958 (Appendix B). It does not to contribute to the interior body
959 force which includes the wave mass flux M_w.

Appendix B: The Nearshore POM

960 POM is a primitive equation model formulated in terrain
961 following σ coordinates [*Blumberg and Mellor*, 1987; *Mel-*
962 *lor*, 2004]. That is, if (x, y, z) are Cartesian coordinates
963 with velocity components (u, v, w) and the variable z sat-
964 isfies $-H \le z \le \eta$, where $\eta = \eta(x, y, t)$ is the sea surface
965 elevation, $H = H(x, y)$ the undisturbed water depth and
966 $D = H + \eta$ is the total depth, the σ vertical coordinate is
967 defined by the transformation

$$\sigma = \frac{z - \eta}{D}, \tag{B1}$$

so that $-1 \leq \sigma \leq 0$ and partial derivatives with respect to (x, y, t) are now calculated with σ held constant.

POM consists of evolution equations for the horizontal velocity components, temperature and salinity concentrations and the turbulence quantities q^2 and $q^2 l$, where q^2 is twice the turbulent kinetic energy and l is a turbulent length scale. Nearshore POM includes the option of using a single equation for potential density in lieu of temperature and salinity and a non-linear equation of state. In this study we ignore the effects of stratification and rotation and will omit these terms from further discussion.

In σ-coordinates, the governing equations in the case of no stratification, are

$$\frac{\partial \eta}{\partial t} + \frac{\partial Du}{\partial x} + \frac{\partial Dv}{\partial y} + \frac{\partial \omega}{\partial \sigma} = 0, \tag{B2}$$

$$\frac{\partial Du}{\partial t} + \frac{\partial Du^2}{\partial x} + \frac{\partial Duv}{\partial y} + \frac{\partial u\omega}{\partial \sigma} + gD\frac{\partial \eta}{\partial x} = \frac{\partial}{\partial \sigma}\frac{K_M}{D}\frac{\partial u}{\partial \sigma} + G_x + DF_b^x, \tag{B3}$$

$$\frac{\partial Dv}{\partial t} + \frac{\partial Duv}{\partial x} + \frac{\partial Dv^2}{\partial y} + \frac{\partial v\omega}{\partial \sigma} + gD\frac{\partial \eta}{\partial y} = \frac{\partial}{\partial \sigma}\frac{K_M}{D}\frac{\partial v}{\partial \sigma} + G_y + DF_b^y, \tag{B4}$$

(u, v) are the (x, y) components of the velocity, respectively, and ω is a velocity component normal to σ surfaces given by

$$\omega = w - u\left(\sigma\frac{\partial D}{\partial x} + \frac{\partial \eta}{\partial x}\right) - v\left(\sigma\frac{\partial D}{\partial y} + \frac{\partial \eta}{\partial y}\right) - \left(\sigma\frac{\partial D}{\partial t} + \frac{\partial \eta}{\partial t}\right). \tag{B5}$$

An additional equation used to calculate η is obtained from the depth-average of (B2)

$$\frac{\partial \eta}{\partial t} + \frac{\partial DU}{\partial x} + \frac{\partial DV}{\partial y} + \omega(0) = 0. \tag{B6}$$

The terms designated G_x and G_y represent the small horizontal mixing. The depth-independent body force terms, F_b^x and F_b^y derived in NA1 are given by

$$F_b^x = -\frac{1}{2}\frac{\partial}{\partial x}\left(\frac{E}{D}\right) + \frac{M_w^y}{D}\left(\frac{\partial V}{\partial x} - \frac{\partial U}{\partial y}\right), \tag{B7}$$

$$F_b^y = -\frac{1}{2}\frac{\partial}{\partial y}\left(\frac{E}{D}\right) - \frac{M_w^x}{D}\left(\frac{\partial V}{\partial x} - \frac{\partial U}{\partial y}\right), \tag{B8}$$

where (U, V) are the depth-averaged components of the velocity, E is the wave energy density obtained from the wave model and (M_w^x, M_w^y) are the components of the wave mass flux.

Surface boundary conditions for these equations are

$$\omega = \omega_s \equiv \frac{\partial M^x}{\partial x} + \frac{\partial M^y}{\partial y} \quad \text{at } \sigma = 0, \tag{B9}$$

where

$$M^x = M_w^x + M_r^x, \qquad M^y = M_w^y + M_r^y. \tag{B10}$$

In addition, for (B3) and (B4),

$$(u\omega, v\omega) = (u\omega_s, v\omega_s) \quad \text{at } \sigma = 0, \tag{B11}$$

and

$$\frac{K_M}{D}\frac{\partial(u,v)}{\partial\sigma} = \frac{(\tau^{sx}, \tau^{sy})}{\rho}, \qquad \text{at } \sigma = 0. \tag{B12}$$

where τ^{sx} and τ^{sy} are the components of the applied surface stress. Without rollers

$$\frac{(\tau^{sx}, \tau^{sy})}{\rho} = (k^x, k^y)\frac{\varepsilon_d}{\omega_r} + \frac{(\tau^{wx}, \tau^{wy})}{\rho}, \tag{B13}$$

where the wavenumber (k^x, k^y), frequency ω_r and dissipation ε_d come from the wave model, (τ^{wx}, τ^{wy}) are the components of the wind stress and ρ is the constant density. With rollers

$$\frac{(\tau^{sx}, \tau^{sy})}{\rho} = (k^x, k^y)\frac{\varepsilon_d}{\omega_r} + [(S_{xxr})_x + (S_{xyr})_y, \\ (S_{yyr})_y + (S_{xyr})_x] + \frac{(\tau^{wx}, \tau^{wy})}{\rho}. \tag{B14}$$

At the bottom

$$\omega = 0 \qquad \text{at } \sigma = -1, \tag{B15}$$

$$\frac{K_M}{D}\frac{\partial(u,v)}{\partial\sigma} = \frac{(\tau^{bx}, \tau^{by})}{\rho}, \qquad \sigma \to -1, \tag{B16}$$

where τ^{bx} and τ^{by} are the components of the bottom stress. The vertical eddy coefficient K_M comes from the turbulence closure.

If the *Mellor* [2002] parameterization for the wave-current bottom boundary layer is used

$$\frac{(\tau^{bx}, \tau^{by})}{\rho} = C_d(u_r^2 + v_r^2)^{\frac{1}{2}}(u_r, v_r), \tag{B17}$$

where u_r and v_r are evaluated at the grid point nearest the bottom located a distance z_r above the bed. The drag coefficient

$$C_d = \max\left[\kappa^2\left[\ln\{1 + z_r/z_b\}\right]^{-2}, 0.0025\right], \tag{B18}$$

where κ is the von Karman constant and z_b is the bottom roughness length. This formulation is a modification of that in POM [*Blumberg and Mellor*, 1987] to correct for the case that the bottom grid point is closer to the bottom than the roughness length z_b. In the Mellor formulation the wave-current interactions in the wave BBL are parametrized by an additional production term for turbulent kinetic energy which modifies the value of the eddy coefficients. If the *Styles and Glenn* [2000, 2002] formulation is used, the bottom stress is calculated within the submodel and includes the wave effects directly.

Momentum balance terms for the momentum equations (B3) and (B4) are calculated with all terms written on the left-hand side of the equation and normalized by the depth D so that, for example, the across-shore advection term is given by

$$\text{ADV} = \frac{1}{D}\left[\frac{\partial Du^2}{\partial x} + \frac{\partial Duv}{\partial y} + \frac{\partial u\omega}{\partial\sigma}\right]. \tag{B19}$$

A turbulence closure is required for the calculation of the parameterized Reynolds stress terms involving the eddy coefficient K_M. POM includes the *Mellor and Yamada* [1982] level 2.5 scheme with the modification of *Galperin et al.*, [1988]. This is a two-equation turbulence closure with equations for q^2, twice the turbulent kinetic energy TKE, and for $q^2 l$, where l is a turbulent length scale:

$$\frac{\partial q^2 D}{\partial t} + \frac{\partial u q^2 D}{\partial x} + \frac{\partial v q^2 D}{\partial y} + \frac{\partial \omega q^2}{\partial \sigma} = \frac{\partial}{\partial \sigma}\frac{K_Q}{D}\frac{\partial q^2}{\partial \sigma} + 2D(P - \varepsilon_q) + G_q, \tag{B20}$$

where K_Q is the mixing coefficient for the turbulent quantities, P and ε_q are the production and dissipation rates of turbulent kinetic energy respectively and G_q is horizontal dissipation. In the case of constant density

$$P = \frac{K_m}{D^2}\left[\left(\frac{\partial u}{\partial \sigma}\right)^2 + \left(\frac{\partial v}{\partial \sigma}\right)^2\right] + P_w, \tag{B21}$$

The term P_w is given by the formula of *Mellor* [2002] if that option for the parameterization of the wave-current interactions in the BBL is chosen and is zero otherwise. The dissipation of TKE is

$$\varepsilon_q = \frac{q^3}{B_1 l}, \tag{B22}$$

where B_1 is an empirical constant [*Mellor and Yamada*, 1982] and l is the length scale obtained from the $q^2 l$ equation:

$$\frac{\partial q^2 l D}{\partial t} + \frac{\partial u q^2 l D}{\partial x} + \frac{\partial v q^2 l D}{\partial y} + \frac{\partial \omega q^2 l}{\partial \sigma} = \frac{\partial}{\partial \sigma}\frac{K_Q}{D}\frac{\partial q^2 l}{\partial \sigma} + E_1 l D P - \frac{D q^3}{B_1}\tilde{W} + G_l, \tag{B23}$$

where $\tilde{W}$, the wall proximity function is given by

$$\tilde{W} \equiv 1 + E_2\left(\frac{l}{\kappa L}\right)^2, \tag{B24}$$

and

$$L^{-1} \equiv (\eta - z + z_s)^{-1} + (H + z + z_b)^{-1}. \tag{B25}$$

where z_s and z_b are the surface and bottom roughness lengths, respectively. Additional empirical constants E_1 and E_2 are required in this formulation [*Mellor and Yamada*, 1982]. In the equations for the turbulent quantities, the centered difference approximation for the advection terms in POM has been replaced by the positive definite scheme of *Smolarkiewicz* [1984].

The original surface boundary conditions in POM are

$$q^2 = B_1^{2/3} u_\star^2, \qquad q^2 l = 0, \tag{B26}$$

where $u_\star$ is the turbulent friction velocity determined from the imposed surface stress, i.e., from the wind stress and B_1 is a constant determined in the derivation of the turbulent closure [*Mellor and Yamada*, 1982]. Following *Craig and Banner* [1994] we replace these boundary conditions at the

surface by

$$\frac{K_Q}{D}\frac{\partial q^2}{\partial \sigma} = 2\alpha u_\star^3, \quad q^2 l = q^2 z_s, \tag{B27}$$

where $u_\star$ is the turbulent friction velocity calculated from the imposed surface stress arising from wave breaking,

$$u_*^2 = \frac{(\tau^{sx2} + \tau^{sy2})^{1/2}}{\rho}, \tag{B28}$$

$\alpha = 100$ is a specified constant determined from observations in deep water, and the vertical eddy coefficient for q^2 is K_Q. The appropriateness of this formulation and the value of the constant α for use within the surf zone are questionable, but this formulation allows the approximation of an increase in turbulence under breaking waves.

Other turbulence closures have been used in the POM model in coastal modeling [*Wijesekera et al.*, 2003] and can be adapted for use in the surf zone if appropriate. An additional issue not addressed here is that of the advection of scalars, such as the turbulence quantities, (B3) and (B4), by the Stokes velocity [*McWilliams et al.*, 2004]. We have assumed this effect to be small and have not implemented it in this version of the model. The vertical eddy coefficients K_M for momentum and K_Q for the turbulent quantities q^2 and $q^2 l$ are calculated as in POM, [*Mellor and Yamada*, 1982; *Galperin et al.*, 1988].

The boundary conditions used are no normal flow at vertical walls located at the offshore and onshore boundaries. The depth at the onshore boundary is 10 cm or less. The offshore boundary is located 1 km offshore, well away from the region of interest, with typical depths of 10-12 m. With the closed boundary offshore, mass conservation requires that the Eulerian wave mass flux that enters the interior in the surf zone at the mean free surface as a vertical flux through boundary condition (B9) be balanced by an appropriate vertical flux out of the interior near the offshore boundary. This is achieved by tapering the wave mass flux M_w^x to zero at the offshore boundary exponentialy over a distance of 50 m.

Acknowledgments. This research was supported by the National Oceanographic Partnership Program (NOPP) through ONR grant N00014-99-1-1051 and by the Office of Naval Research (ONR) Coastal Dynamics Program under grant N00014-02-1-0100. We thank the other NOPP project investigators, in general, for very helpful interactions. In particular, we thank E.B. Thornton for the sled velocity measurements, S. Elgar and R. Guza for the fixed array velocity measurements, and H.T. Özkan-Haller for the code for the wave model and for useful discussions. In addition, we are especially grateful to F. Feddersen for providing processed fixed array data, windstress and topography, and the software to calculate optimal wave transformation parameters. We also gratefully acknowledge benefiting from the bathymetry, wind and 8 m depth pressure array measurements provided by the Field Research Facility (FRF), Coastal Engineering Research Center, Duck, NC.

References

Allen, J. S., P. A. Newberger and R. A. Holman (1996), Nonlinear shear instabilities of alongshore currents on plane beaches, *J. Fluid Mech.*, *310*, 181-213.

Ardhuin, F., T.H.C. Herbers and W.C. O'Reilly (2003), Swell transformation across the continental shelf. Part 1: Attenuation and directional broadening, *J. Phys. Oceanogr.*, *33*, 1921-1939.

Blumberg, A. F. and G. L. Mellor (1987), A description of a three-dimensional coastal ocean circulation model, In *Three-Dimensional Coastal Ocean Models*, N. S. Heaps (Ed.), American Geophysical Union, Washington, DC, 1-16.

Burchard, H. (2001), Simulation the wave-enhanced layer under breaking surface waves with two-equation turbulence models, *J. Phys. Oceanogr.*, *31*, 3133-3145.

Church, J.C. and E.B. Thornton (1993), Effects of breaking wave induced turbulence within a longshore current model, *Coastal Engrg.*, *20*, 1-28.

Craig, P.D. and M.L. Banner (1994), Modeling wave-enhanced turbulence in the ocean surface layer, *J. Phys. Oceanogr.*, *24*, 2546-2559.

Dally W.R. and Brown C.A. (1995), A modeling investigation of the breaking wave roller with application to cross-shore currents, *J. Geophys. Res.*, *100*, 24,873-24,883.

Deigaard, R. (1993), A note on the three-dimensional shear stress distribution in a surf zone. *Coastal Engrg.*, *20*, 157-171.

Elgar, S., T.H.C. Herbers, and R.T. Guza (1994), Reflection of ocean surface gravity waves from a natural beach, *J. Phys. Oceanogr.*, *24*, 1503-1511.

Feddersen, F., R.T. Guza and S. Elgar (2004), Inverse modeling of one-dimensional setup and alongshore current in the nearshore, *J. Phys. Oceanogr.*, *34*, 920-933.

Feddersen, F., R.T. Guza, S. Elgar and T.H.C. Herbers (1998), Alongshore momentum balances in the nearshore, *J. Geophys. Res.*, *103*, 15,667-15,676.

Feddersen, F., E.L. Gallagher, R.T. Guza and S. Elgar (2003), The drag coefficient, bottom roughness, and wave-breaking in the nearshore, *Coastal Engrg.*, *48*, 189-195.

Gallagher, E.L., W. Boyd, S. Elgar, R.T. Guza and B. Woodward (1996), Performance of a sonar altimeter in the neearshore, *Mar. Geol.*, *133*, 241-248.

Galperin, B., L.H. Kantha, S. Hassid and A. Rossati (1988), A quasi-equilibrium turbulent energy model for geophysical flows, *J. Atmos. Sci.*, *45*, 55-62.

Garcez Faria, A.F., E.B. Thornton, T.P. Stanton, C.V. Soares and t.c. Lippmann (1998), Vertical profiles of longshore currents and related bed stress and bottom roughness, *J. Geophys. Res.*, *103*, 15,667-15,676.

Garcez Faria, A.F., E.B. Thornton, T.C. Lippmann and T.P. Stanton (2000), Undertow over a barred beach, *J. Geophys. Res.*, *105*, 16,999-17,010.

Gemmrich, J.R. and D.M. Farmer (1999), Near-surface turbulence and thermal structure in a wind-driven sea, *J. Phys. Oceanogr.*, *29*, 480-499.

Grant, W.D. and O.S. Madsen (1979), Combined wave and current interaction with a rough bottom, *J. Geophys. Res.*, *89*, 1797-1808.

Haas, K.A., I.A. Svendsen, M.C. Haller and Q. Zhao (2003), Quasi-three-dimensional modeling of rip current systems, *J. Geophys. Res.*, *108* (C7),3217,doi:10.1029/2002JC001355.

Hasselmann, K. (1971), On the mass and momentum transfer between short gravity waves and larger-scale motions, *J. Fluid Mech.*, *50*, 189-205.

Lentz, S., R.T. Guza, S. Elgar, F. Feddersen and T.H.C. Herbers (1999), Momentum balances on the North Carolina inner shelf, *J. Geophys. Res*, *104*, 18,205-18,226.

Longuet-Higgins, M.S. (1973), The mechanics of the surf zone, Proc. 13th Int'l Congress on Theor. and Appl. Mech., Moscow, 1972, edited by E. Becker and G.K. Mikhailov, Springer-Verlag, New York, 213-228.

Longuet-Higgins, M.S. and R.W. Stewart (1964), Radiation stress in water waves; a physical discussion, with application,. *Deep Sea Res.*, *11*, 529-562.

McWilliams, J.C., J.M. Restrepo and E.M. Lane (2004), An asymptotic theory for the interaction of waves and currents in coastal waters, *J. Fluid Mech.*, *511*, 135-178.

Madsen, O.S., P.P. Mathisen and M.M. Rosengaus (1991), Movable bed friction factors for spectral waves, *Proc. Coastal Engineering 1990*, ASCE, 420-439.

Mellor, G.L. (2002), Oscillatory bottom boundary layers, *J. Phys. Oceanogr.*, *32*, 3075-3088.

Mellor, G.L. (2004), USERS GUIDE for a three-dimensional, primitive equation, numerical ocean model, Program in Atmos. and Ocean. Sci., Princeton, University, 56pp.

Mellor, G.L. and A.F. Blumberg (2004), Wave breaking and ocean surface layer thermal response, *J. Phys. Oceanogr.*, *34*, 693-698.

Mellor, G.L. and T. Yamada (1982), Development of a turbulence closure model for geophysical fluid problems, *Rev. Geophys.*, *20*, 851-875.

Nairn, R.B., J.A. Roelvink and H.N. Southgate (1991), *Proc. Coastal Engineering 1990*, ASCE, 68-81.

Newberger, P.A. and J.S. Allen (2007), Forcing a three-dimensional, hydrostatic primitive-equation model for application in the surf zone, Part 1: Formulation, submitted to *J. Geophys. Res.*

Noyes, T.J., R.T. Guza, S. Elgar and T.H.C. Herbers (2004), Field observations of shear waves in the surf zone. *J. Geophys. Res.*, *109*, C01031, doi:10.1029/2002JC001761.

Oltman-Shay, J., P.A. Howd and W.A. Birkemeier (1989), Shear instabilities of the mean longshore current: 2. Field Observations. *J. Geophys. Res.*, *94*, 18,031-18,042.

Özkan, H.T and J.T. Kirby (1999), Nonlinear evolution of shear instabilities of the longshore current: A comparison of observations and computations. *J. Geophys. Res.*, *104*, 25,953-25,984.

Özkan-Haller, H.T. and Y. Li (2003), Effects of wave-current interaction on shear instabilities of longshore currents. *J. Geophys. Res*, *108* (C5), 3139, doi:10.1029/2001JC001287.

Putrevu, U. and I.A. Svendsen (1999), Three-dimensional dispersion of momentum in wave-induced nearshore currents., *Eur. J. Mech. B/Fluids*, *18*, 409-427.

Reniers, A.J.H.M., and J.A. Battjes (1997), Non-linear modelling of shear instabilities, *Proc. Coastal Dynamics 1997*, ASCE, 436-445.

Reniers, A.J.H.M., J.A. Roelvink and E.B. Thornton (2004), Morphodynamic modeling of an embayed beach under wave group forcing, *J. Geophys. Res. 109*, C01030, doi:10.1029/2002JC001586.

Reniers, A.J.H.M., J.A. Battjes, A. Falques and D.A. Huntley (1997), A laboratory study on the shear instability of longshore currents, *J. Geophys. Res.*, *102*, 8597-8609.

Reniers, A.J.H.M., A.R. Van Dongeren, J.A. Battjes and E.B. Thornton (2002), Linear modeling of infragravity waves during Delilah. *J. Geophys. Res.*, *107* (C10), 3137, doi:10.1029/2001JC001083.

Shi, F., J.T. Kirby, P.A. Newberger and K. Haas (2005), NearCoM master program, version 2005.4, User's manual and module integration, Research Report, Center for Applied Coastal Research, University of Delaware.

Slinn, D.N., J.S. Allen, P.A. Newberger and R.A. Holman (1998), Nonlinear shear instabilities of alongshore currents over barred beaches, *J. Geophys. Res. 103*, 18,357-18,379.

Smith, J.A. (2006), Wave-current interactions in finite-depth, *J. Phys. Oceanogr.*, *36*, 1403-1419.

Smolarkiewicz, P.K. (1984), A fully multidimensional positive definite advection transport algorithm with small implicit diffusion, *J. Comp. Phys.*, *54*, 325-562.

Stive, M.J.F. and H.J. De Vriend (1995), Shear stresses and mean flow in shoaling and breaking waves, in *Proc. Coastal Engineering 1994*, ASCE, 594-608.

Styles, R. and S.M. Glenn (2000), Modeling stratified wave and current bottom boundary layers on the continental shelf, *J. Geophys. Res.*, *105*, 24,119-24,139.

Styles, R. and S.M. Glenn (2002), An optimized combined wave and current algorithm for arbitrary bed roughness, Boundary Layer Stress and Sediment Transport Laboratory, Dept. of Geological Sciences, University of South Carolina, Columbia, 34pp.

Svendsen, I.A. (1984), Mass flux and undertow in a surf zone, *Coastal Engrg.*, *8*, 347-365.

Svendsen, I.A. and U. Putrevu (1994), Nearshore mixing and dispersion, *Proc. R. Soc. London*, Ser. A, *445*, 561-576.

Thornton, E.B. and R.T. Guza (1983), Transformations of wave height distribution, *J. Geophys. Res*, *88*, 5925-5938.

Thornton, E.B. and R.T. Guza (1986), Surf zone longshore currents and random waves: field data and models, *J. Phys. Oceanogr.*, *16*, 1165-1178.

Thornton, E.B. and C.S. Kim (1993), Longshore current and wave height modulation at tidal frequency inside the surf zone, *J. Geophys. Res.*, *98*, 16,509-16,519.

Thornton, E.B. and D.J. Whitford (1990), Longshore currents over a barred beach: Part II, Model, Naval Postgraduate School, Monterey, 30pp.

Van Dongeren, A.R., F.E. Sancho, I.A. Svendsen and U. Putrevu (1995), SHORECIRC: A quasi 3-D nearshore model, *Proc. Coastal Engineering 1994*, ASCE, 2741-2754.

Wijesekera, H.W., J.S. Allen and P.A. Newberger (2003), Modeling study of turbulent closure schemes, *J. Geophys. Res.*, *108* (C3), 3103, doi:10.1029/2001JC001234.

Zhao, Q., I.A. Svendsen and K. Haas (2003), Three-dimensional effects in shear waves, *J. Geophys. Res.*, *108* (C8), 3270, doi:10.1029/2002JC001306.

P. A. Newberger and J.S. Allen, College of Oceanic and Atmospheric Sciences, Oregon State University, 104 Ocean Admin Bldg, Corvallis, OR, 97331-5503, USA. (newberg@coas.oregonstate.edu, jallen@coas.oregonstate.edu)

(Received _____.)

Figure 1. Wave heights and topography for Sled Run 4. The circles are wave height infered from data from the fixed array and 8 m isobath mooring. The solid line in the top panel is wave heights calculated from the wave model solution for Sled Run 4, Experiment 11 (Tables 1 and 2). In this and other figures the x axis label, FRF coordinate, refers to the distance offshore from the FRF defined $x = 0$, not to the orientation of the coordinate system as in Table 2.

Figure 2. Sled Run 4, Experiment 11: Fields of velocity components u and v, $q^2 = 2 \times$ TKE, and vertical eddy coefficient K_M (Appendix B). The contour intervals are $\Delta(u, v) = 0.1$ m s^{-1} with heavy contours at ± 0.5 m s^{-1}, $\Delta(q^2) = 0.05$ m^2 s^{-2} with contours above 0.4 m^2 s^{-2} omitted for clarity, $\Delta(K_M) = 0.01$ m^2 s^{-1}. For the across-shore velocity u, values greater than or equal to zero are indicated by solid contours, negative values are indicated by dashed contours. For the alongshore velocity v, negative values are indicated by solid contours.

Figure 3. Sled Run 4, Experiment 11: Depth-dependent momentum balances. Contour intervals are $\Delta = 0.002$ m s^{-2} for the x balances and $\Delta = 0.001$ m s^{-2} for the y balances. Values greater than or equal to zero are indicated by solid contours, negative values are indicated by dashed contours.

Figure 4. Sled Run 4, Experiments 11 (left) and 16 (right): Top: Depth-averaged velocities U, V (m s^{-1}) and surface elevation η (m). Center: Across-shore x depth-averaged momentum balance. Bottom: Alongshore y depth-averaged momentum balance.

Figure 5. Sled Run 4, Experiment 16: Fields of velocity components u and v, $q^2 = 2 \times$ TKE, and vertical eddy coefficient K_M (Appendix B). Contour intervals as in Figure 2.

Figure 6. Sled Run 4, Experiment 16: Depth-dependent momentum balances. Contour intervals as in Figure 3.

Figure 7. Sled Run 4, Experiments 18 (left) and 19 (right): Top: Depth-averaged velocities U, V (m s^{-1}) and surface elevation η (m). Center: Across-shore x depth-averaged momentum balance. Bottom: Alongshore y depth-averaged momentum balance.

Figure 8. Comparison of sled velocity measurements (circles) and model velocities (solid lines) for Experiment 11 (top panels) and Experiment 1 (bottom panels). The specification of these experiments is given in Table 2. The zero line for each profile is shown in gray. The tide height changes during the experiment thus the water surface for each run is marked by a solid square.

Figure 9. Composite errors $\tilde{\Xi}$ (2) for the 19 experiments of Table 2. The upper panel shows the errors for the 11 runs examining sensitivity to changes in bottom roughness z_b, surface roughness z_s, choice of BBL (SG or ML) and coordinate system (FRF or ISO) (Table 2). The lower panel examines the effects of including wind, rollers and wave-current interactions in the forcing. Vertical profiles of the two experiments marked with a filled square are shown in Figure 8.

Figure 10. Comparison of u profiles for Run 4 (x=225 m) and Run 6 (x=188 m) of Experiments 1-4 together with the corresponding sled current measurements (circles). The surface roughness length z_s is the only parameter that is changed in these experiments, where z_s=(0.3, 0.2, 0.5, 0.2 H_{rms}) m for experiments (1,2,3,4) respectively (Table 2).

Figure 11. Depth-averaged alongshore velocity V for Sled Run 4 of Experiment 10 in the FRF coordinate system and Experiment 11 in the ISO system.

Figure 12. Comparison of Run 4 from Experiment 11 (top) and Experiment 16 (bottom) with the hourly-averaged velocity data from the fixed array from 1200 h 12 October 1994. Experiment 11 differs from Experiment 16 only in the omission in Experiment 16 of rollers.

Figure 13. Model wave heights and topography for the low, mid and high tide simulations. Low tide is indicated by a solid line, mid tide by a long dash and high tide by a short dash. The across-shore coordinate is such that the location of the shoreline changes with tidal height while the bar location does not.

Figure 14. Depth-averaged alongshore velocity V for the three tide simulations. The location of the maximum current moves on shore with increasing water depth. The maximum V occurs at mid tide.

Figure 15. Vertical profiles of u and v for the low tide and high tide simulations.

Figure 16. Horizontal fields of u (top) and v (bottom) on σ level 2, near the surface for Experiments 1-4 (Table 4). The left most column shows Experiment 1 with the complete linked wave-current model, including both wave-current interaction terms in the wave model and the vortex force term in the circulation model. The other experiments omit one or both of these terms. The contour interval $\Delta = 0.1$ m s^{-1}.

Figure 17. Alongshore averaged $< u >$ and $< v >$ (top) from Experiment 1 at the same time as shown in Figure 16 contrasted with u and v from the corresponding 2D model (row 2). The contour interval $\Delta(u, v) = 0.1$ m s^{-1}. Snap shots of the perturbations u' ($\Delta u' = 0.05$ m s^{-1}) and v' ($\Delta v' = 0.1$ m s^{-1}) at two alongshore locations (rows 3 and 4). For the across-shore velocity u and the perturbation u' and v', values greater than or equal to zero are indicated by solid contours, negative values are indicated by dashed contours. For the alongshore velocity v, negative values are indicated by solid contours.

Figure 18. Horizontal fields of u (top) and v (bottom) on σ level 2, near the surface for Experiments 5-8 (Table 4). Contour intervals as in Figure 16.

Sled	Run 1	Run 2	Run 3	Run 4	Run 5	Run 6	Run 7
local time	8:00	9:30	11:10	12:27	13:40	15:12	16:21
FRF x location (m)	298	273	252	225	210	188	172
wave period (s)	5.7	5.8	5.9	5.9	6.0	6.1	6.2
depth at bar (m)	2.2	2.4	2.8	2.9	2.9	2.7	2.5
H_{rms} (m)	1.34	1.54	1.60	1.57	1.57	1.60	1.66
(isobath)	1.33	1.53	1.59	1.56	1.56	1.59	1.66
Θ (°)	10.0	8.3	7.2	8.1	7.7	6.7	4.5
(isobath)	12.1	10.4	9.3	10.3	9.8	8.8	6.6
$\tau^x_{wind} \times 10^4$ (m^2s^{-2})	-2.62	-2.41	-2.39	-2.47	-2.51	-2.35	-2.28
(isobath)	-2.57	-2.35	-2.34	-2.42	-2.46	-2.30	-2.24
$\tau^y_{wind} \times 10^4$ (m^2s^{-2})	-1.58	-1.50	-1.56	-1.42	-1.42	-1.44	-1.30
(isobath)	-1.67	-1.58	-1.65	-1.51	-1.51	-1.52	-1.38
γ	0.30	0.30	0.31	0.31	0.29	0.32	0.33
(isobath)	0.30	0.30	0.31	0.31	0.30	0.32	0.33
B	0.72	0.68	0.64	0.64	0.59	0.66	0.77
(isobath)	0.72	0.68	0.64	0.64	0.60	0.66	0.77

Table 1. Sled runs and calculated offshore wave properties for 12 October 1994. Below the line, the values entered after the variable are for the FRF coordinate system. The values entered after (isobath) refer to the variable directly above, but are for the ISO (along-isobath) coordinate system.

	z_s (m)	z_b (m)	BBL	roller	θ	wind	wave-current
1	0.3	0.005	ML	yes	FRF	yes	yes
2	0.2	0.005	ML	yes	FRF	yes	yes
3	0.5	0.005	ML	yes	FRF	yes	yes
4	$0.2H_{rms}$	0.005	ML	yes	FRF	yes	yes
5	0.3	0.001	ML	yes	FRF	yes	yes
6	0.3	0.003	ML	yes	FRF	yes	yes
7	0.3	0.005	ML	yes	ISO	yes	yes
8	0.3	0.005	SG	yes	FRF	yes	yes
9	0.5	0.001	SG	yes	FRF	yes	yes
10	0.3	0.001	SG	yes	FRF	yes	yes
11	0.3	0.001	SG	yes	ISO	yes	yes
12	0.3	0.005	ML	yes	FRF	no	yes
13	0.3	0.005	ML	no	FRF	yes	yes
14	0.3	0.005	ML	no	FRF	no	yes
15	0.3	0.001	SG	yes	ISO	no	yes
16	0.3	0.001	SG	no	ISO	yes	yes
17	0.3	0.001	SG	no	ISO	no	yes
18	0.3	0.001	SG	yes	ISO	yes	no
19	0.3	0.001	SG	no	ISO	yes	no

Table 2. Experiments for model-data comparisons. Under BBL, ML indicates the use of the *Mellor* [2002] wave-current bottom boundary layer parameterization (BBLP) and SG indicates the *Styles and Glenn* [2000, 2002] bottom boundary layer model (BBLM). Under θ, the coordinate system, FRF or ISO (along-isobath), is indicated. 'Yes' in the wave-current column indicates that the depth-averaged mean currents are included in the wave model and that the vortex force is included in the circulation model. 'No' in this column indicates that these terms are omitted.

tide	x_{bar}	D_{bar}	u_{bar}	T_{bar}	Δx_u	u_{max}	Δx_v	v_{max}
Low	131	2.1	0.46	0.41	8	0.48	-16	-0.55
Mid	135	2.4	0.49	0.51	6	0.50	-24	-0.57
High	137	2.9	0.51	0.63	4	0.52	-40	-0.55

Table 3. Distance offshore of the bar x_{bar}, water depth D_{bar}, maximum offshore velocity u_{bar}, and offshore transport T_{bar} over the bar. Location relative to the bar Δx_u and magnitude of the maximum offshore velocity u_{max}. Location relative to the bar Δx_v of the strongest alongshore velocity v_{max}.

	z_s (m)	topography	offshore angle	formulation
1	0.5	High tide	20°	wave-current, vortex force
2	0.5	High tide	20°	no wave-current, vortex force
3	0.5	High tide	20°	wave-current, no vortex force
4	0.5	High tide	20°	no wave-current, no vortex force
5	0.2	High tide	20°	wave-current, vortex force
6	$0.3H_{rms}$	High tide	20°	wave-current, vortex force
7	0.5	Low tide	20°	wave-current, vortex force
8	0.5	High tide	15°	wave-current, vortex force

Table 4. Three-dimensional instability experiments. The notation wave-current, or no wave-current, refers, respectively, to the use of the full wave model (Appendix A) or to the wave model with the effects of the currents (U,V) omitted. The notation vortex force, or no vortex force, refers, respectively, to use of the full circulation model or to the circulation model with the vortex force terms (the wave-current interaction terms in (B7) and (B8)) omitted.

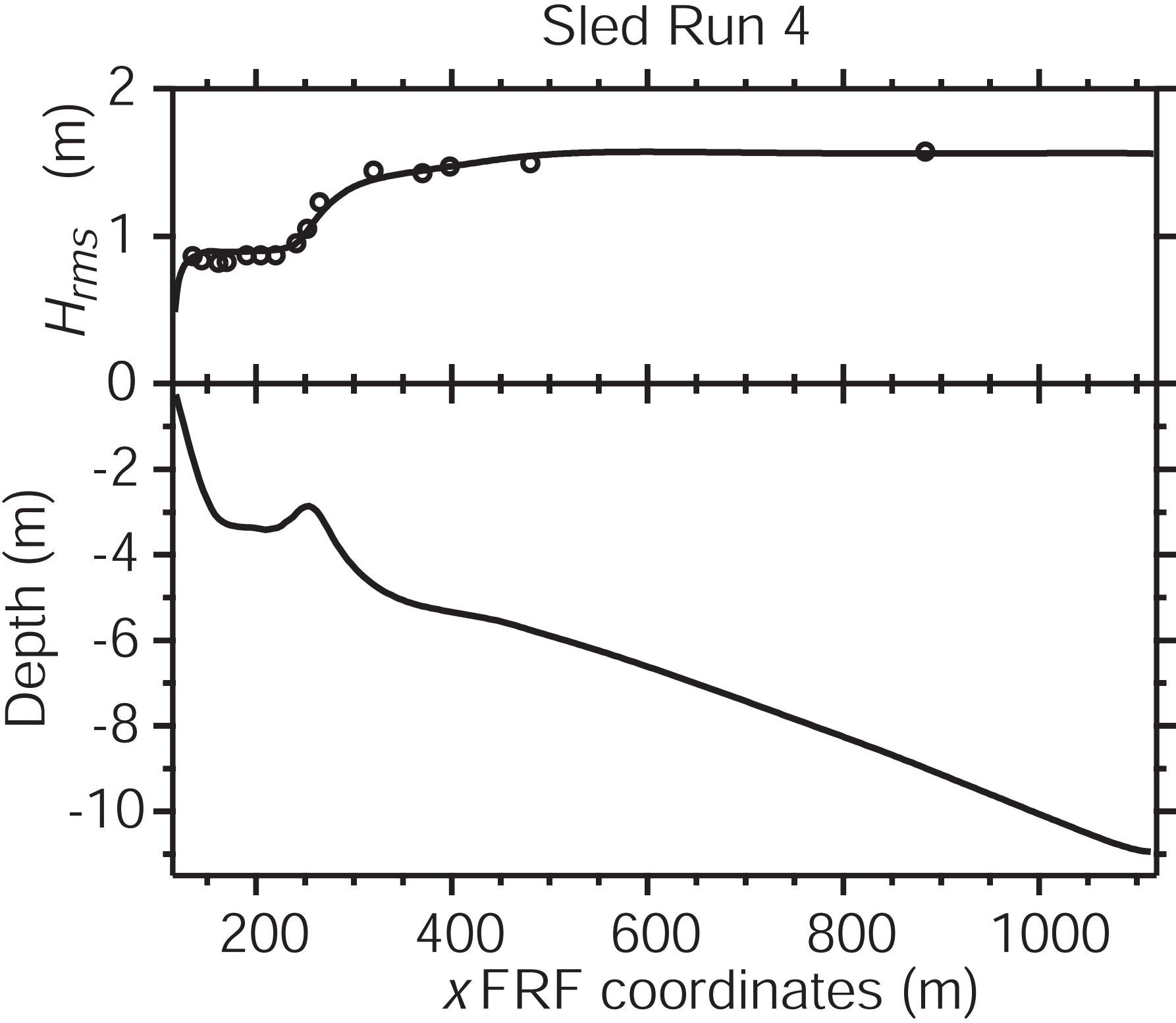
Sled Run 4
H_{rms} (m)
2
1
0
Depth (m)
-2
-4
-6
-8
-10
200
400
600
800
1000
x FRF coordinates (m)

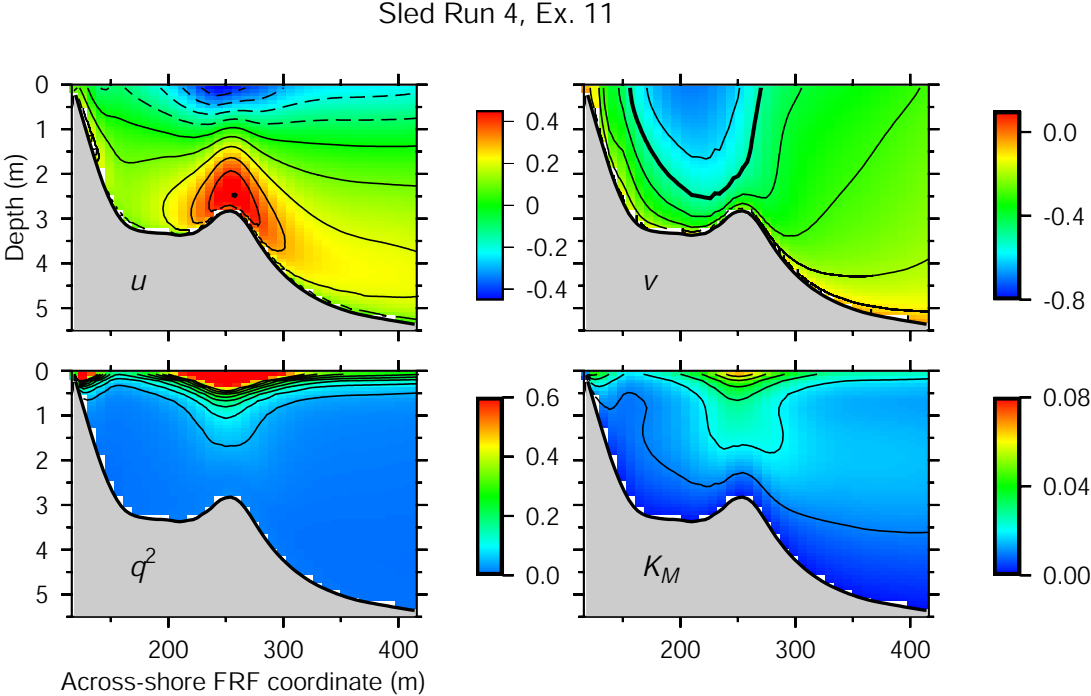
Sled Run 4, Ex. 11
Depth (m)
0
1
2
3
4
5
u
0.4
0.2
0
-0.2
-0.4
v
0.0
-0.4
-0.8
q2
0.6
0.4
0.2
0.0
KM
0.08
0.04
0.00
200
300
400
Across-shore FRF coordinate (m)

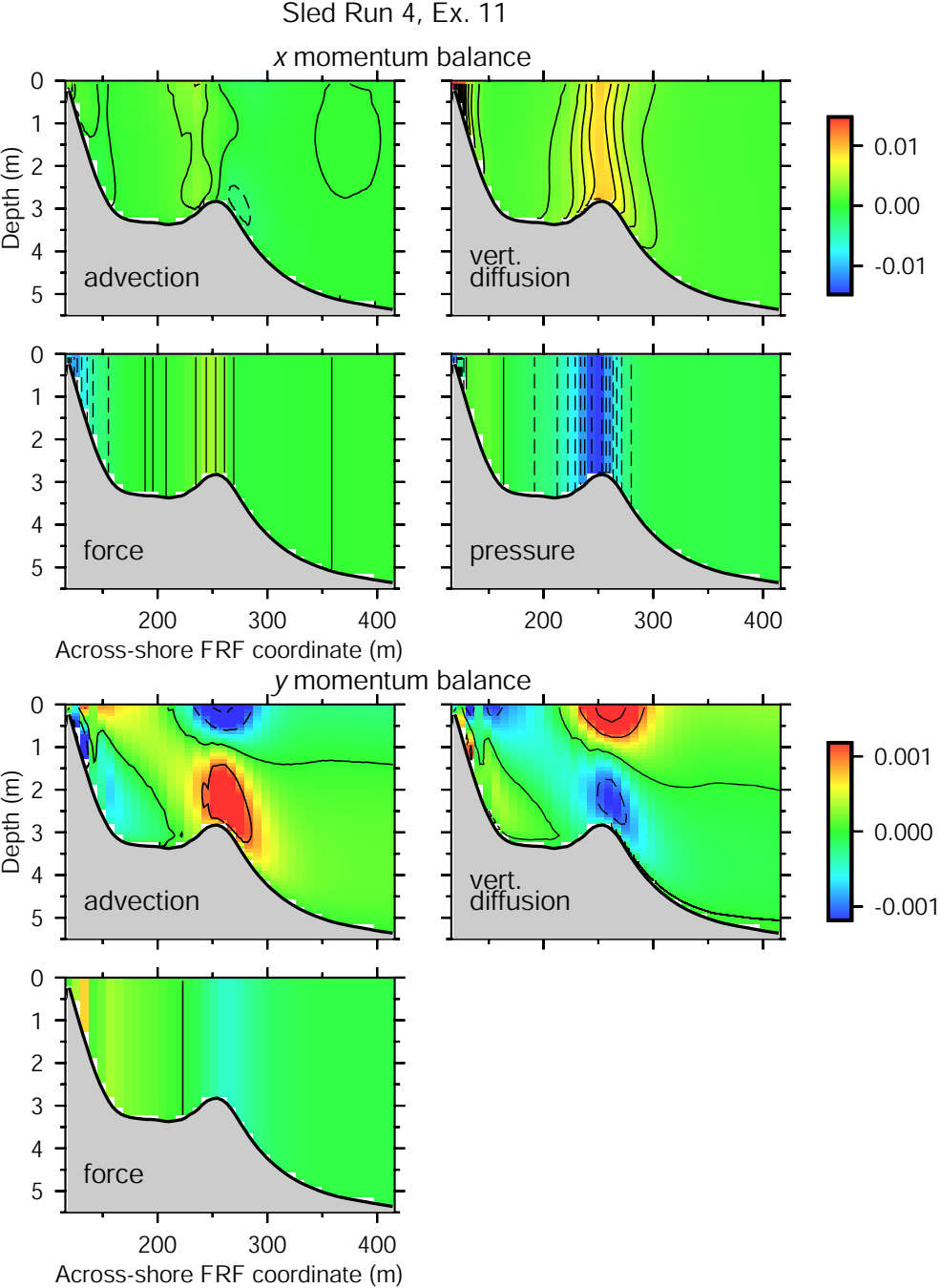
Sled Run 4, Ex. 11
x momentum balance
Depth (m)
advection
vert.
diffusion
force
pressure
0.01
0.00
-0.01
Across-shore FRF coordinate (m)
y momentum balance
Depth (m)
advection
vert.
diffusion
force
0.001
0.000
-0.001
Across-shore FRF coordinate (m)

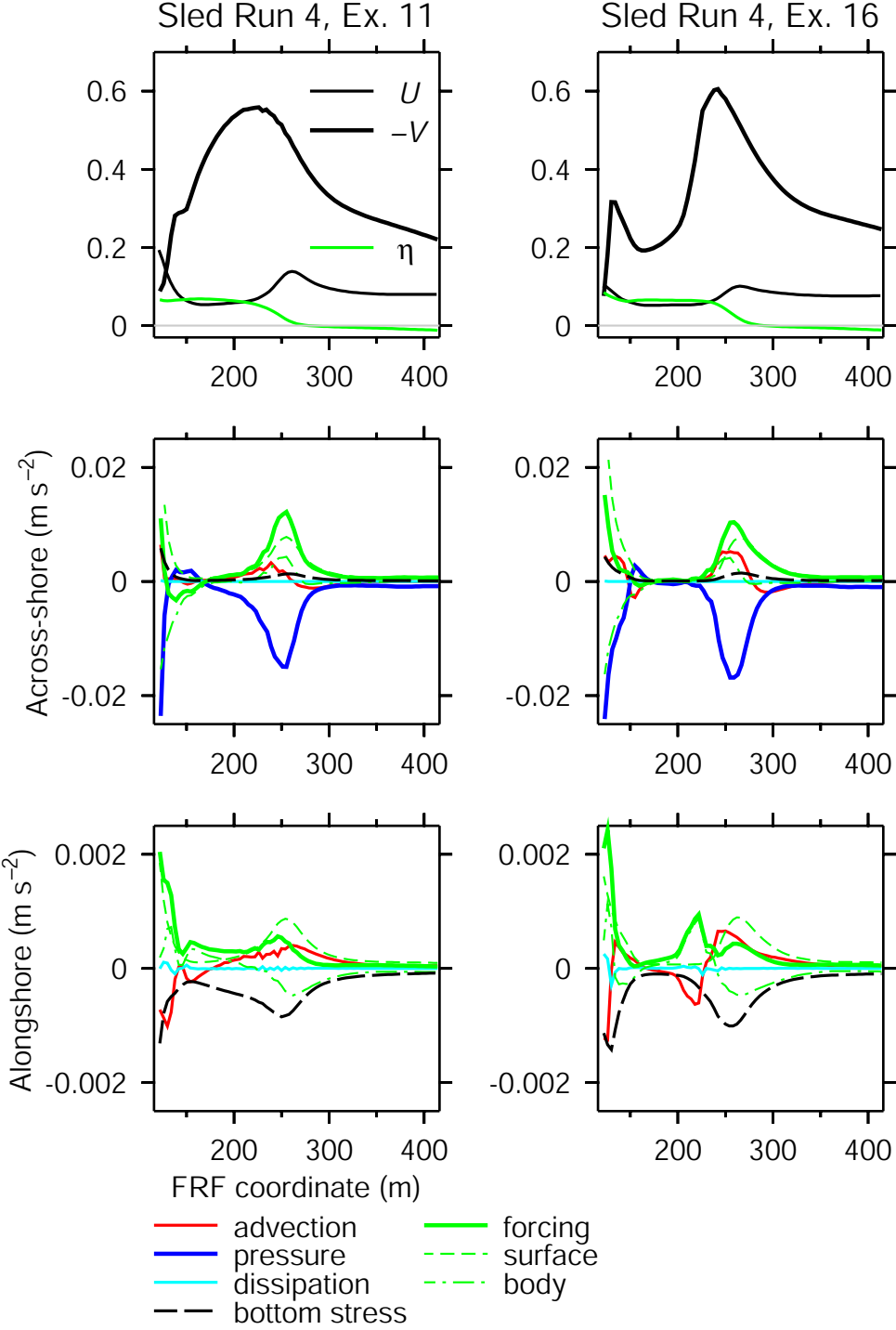
Sled Run 4, Ex. 11
Sled Run 4, Ex. 16
U
–V
η
0.6
0.4
0.2
0
200
300
400
0.02
0
-0.02
Across-shore (m s^{-2})
0.002
-0.002
Alongshore (m s^{-2})
FRF coordinate (m)
advection
pressure
dissipation
bottom stress
forcing
surface
body

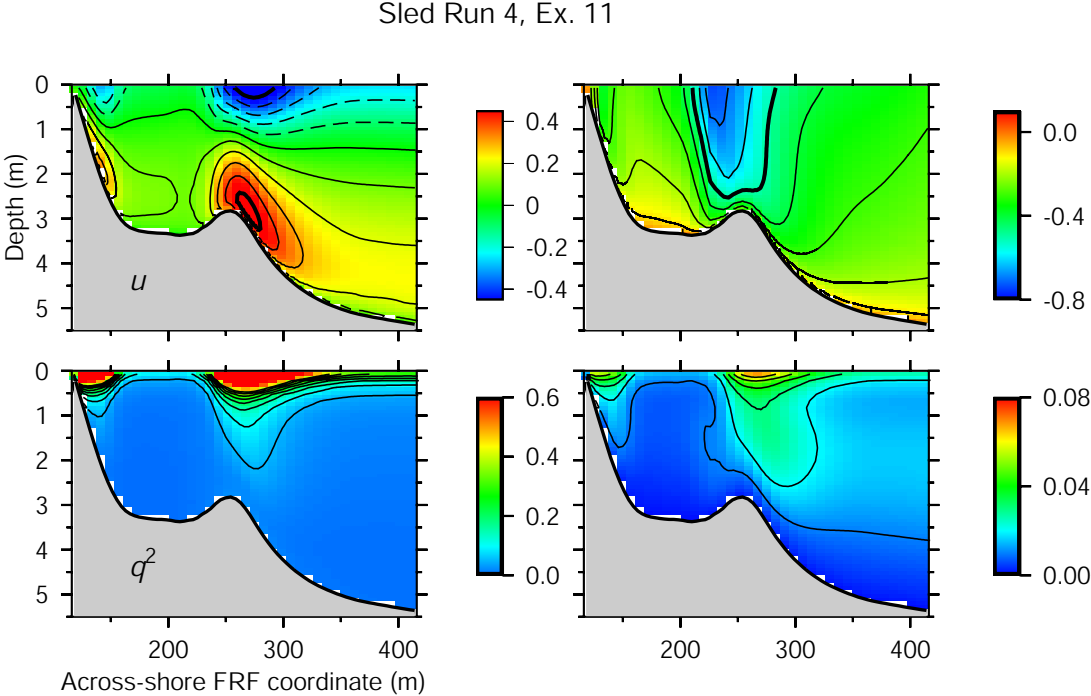
Sled Run 4, Ex. 11
Depth (m)
0
1
2
3
4
5
u
0.4
0.2
0
-0.2
-0.4
0.0
-0.4
-0.8
q2
0.6
0.4
0.2
0.0
0.08
0.04
0.00
200
300
400
Across-shore FRF coordinate (m)

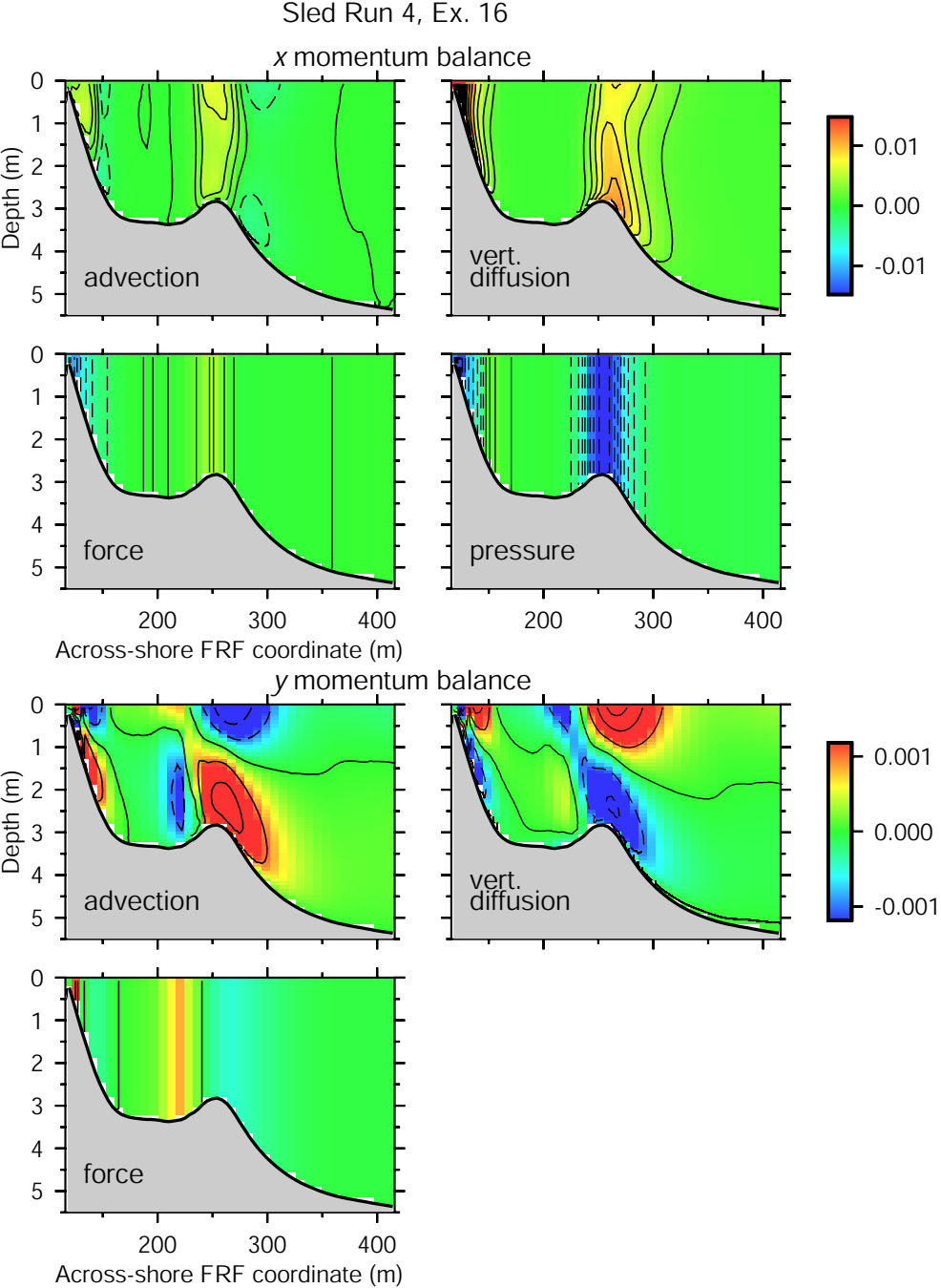
Sled Run 4, Ex. 16
x momentum balance
Depth (m)
advection
vert.
diffusion
force
pressure
0.01
0.00
-0.01
200
300
400
Across-shore FRF coordinate (m)
y momentum balance
Depth (m)
advection
vert.
diffusion
force
0.001
0.000
-0.001
200
300
400
Across-shore FRF coordinate (m)

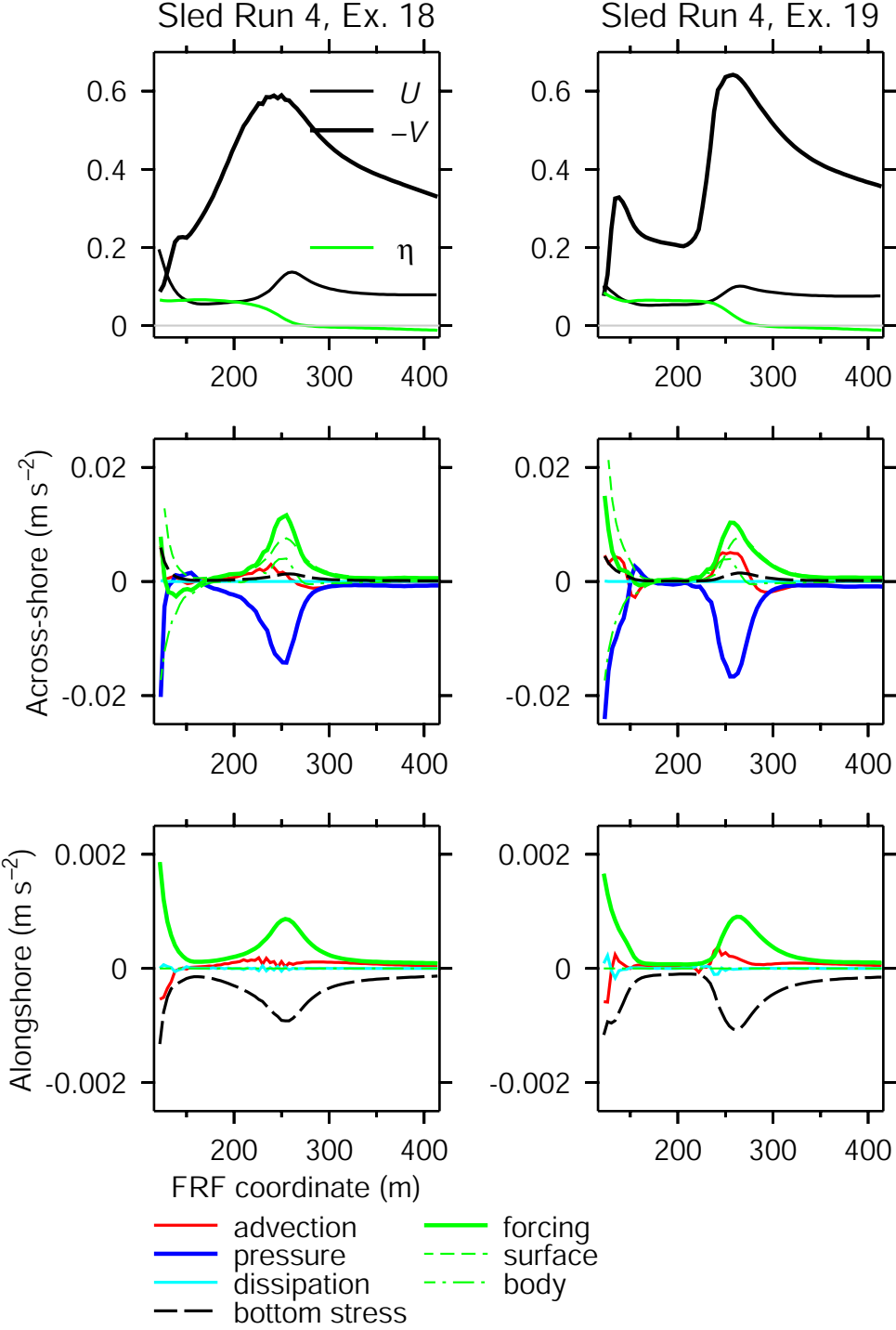
Sled Run 4, Ex. 18
Sled Run 4, Ex. 19
U
−V
η
0.6
0.4
0.2
0
200
300
400
0.02
0
-0.02
Across-shore (m s−2)
0.002
-0.002
Alongshore (m s−2)
FRF coordinate (m)
advection
pressure
dissipation
bottom stress
forcing
surface
body

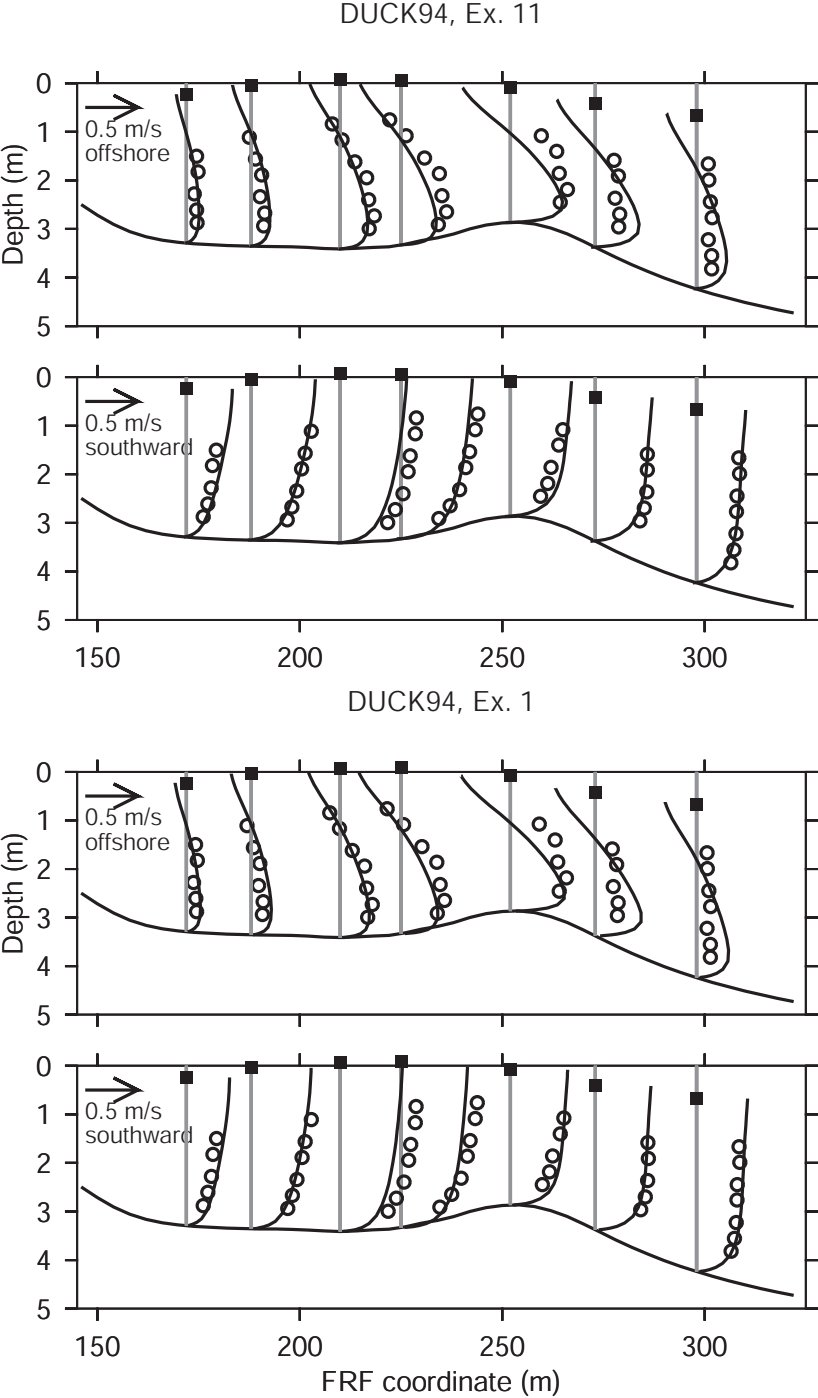
DUCK94, Ex. 11
Depth (m)
0.5 m/s
offshore
0.5 m/s
southward
DUCK94, Ex. 1
Depth (m)
0.5 m/s
offshore
0.5 m/s
southward
FRF coordinate (m)

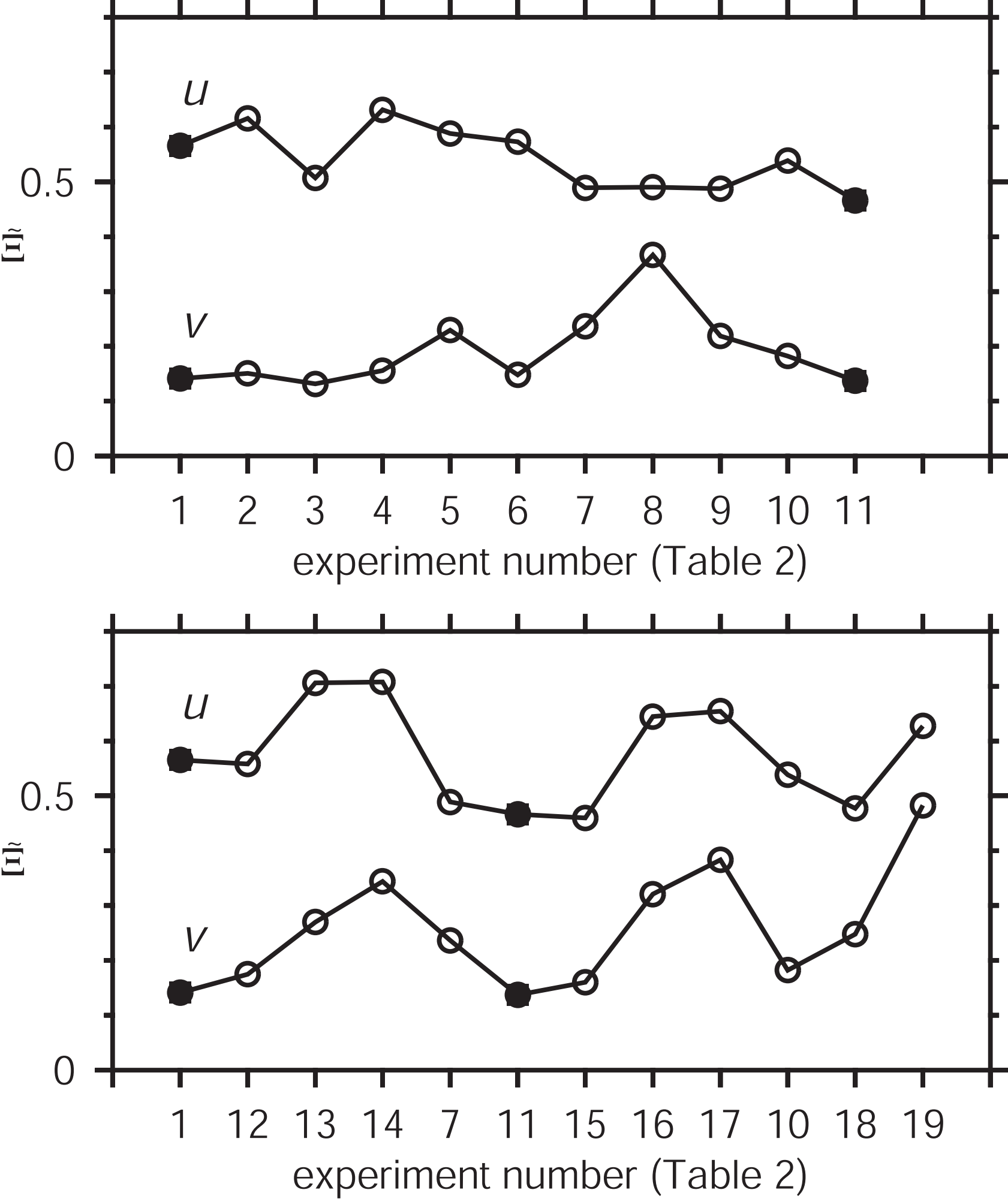
u
v
0.5
0
[r]~
1 2 3 4 5 6 7 8 9 10 11
experiment number (Table 2)
u
v
0.5
0
[r]~
1 12 13 14 7 11 15 16 17 10 18 19
experiment number (Table 2)

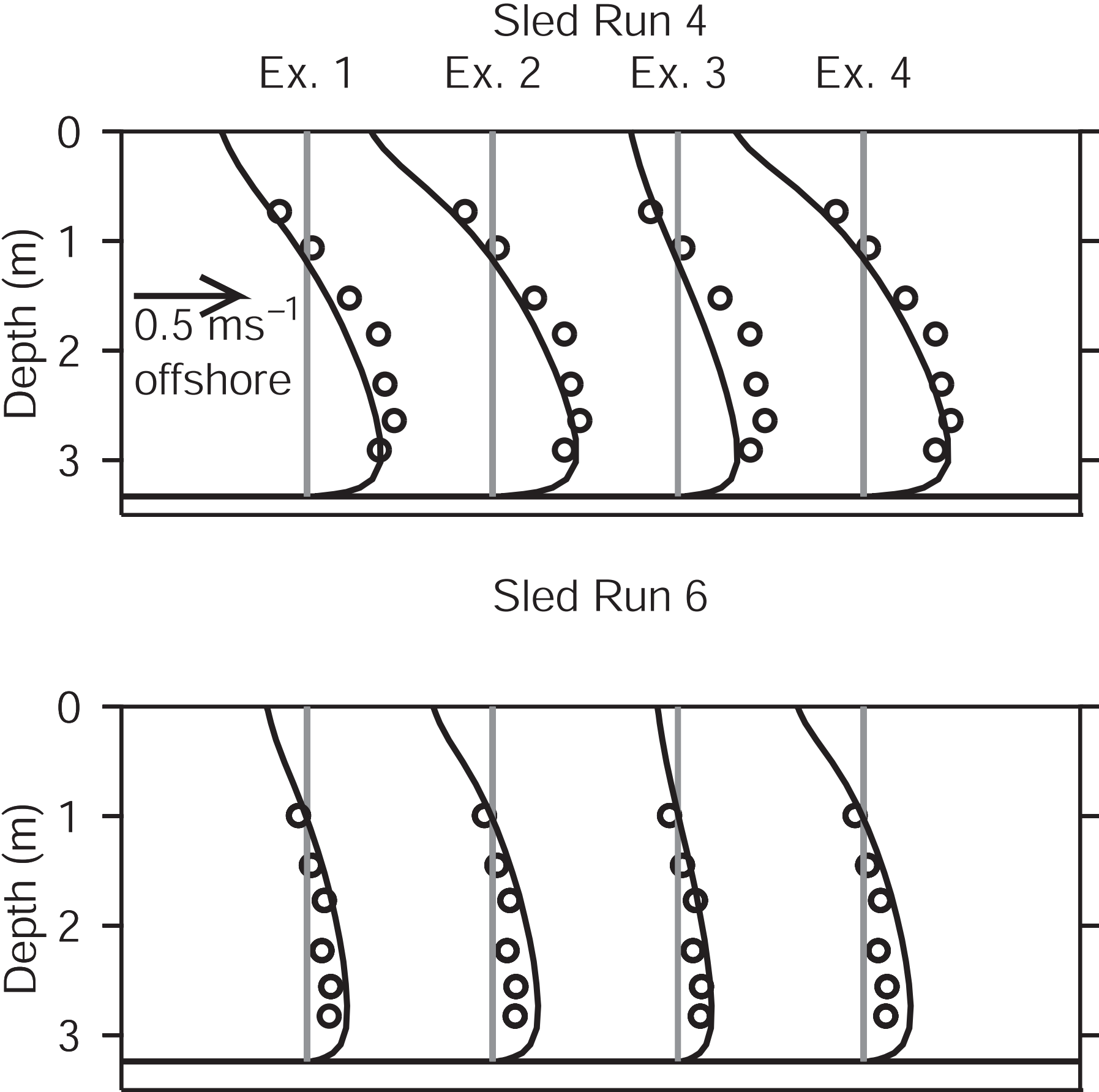
Sled Run 4
Ex. 1
Ex. 2
Ex. 3
Ex. 4
Depth (m)
0
1
2
3
0.5 ms^{-1}
offshore
Sled Run 6
Depth (m)
0
1
2
3

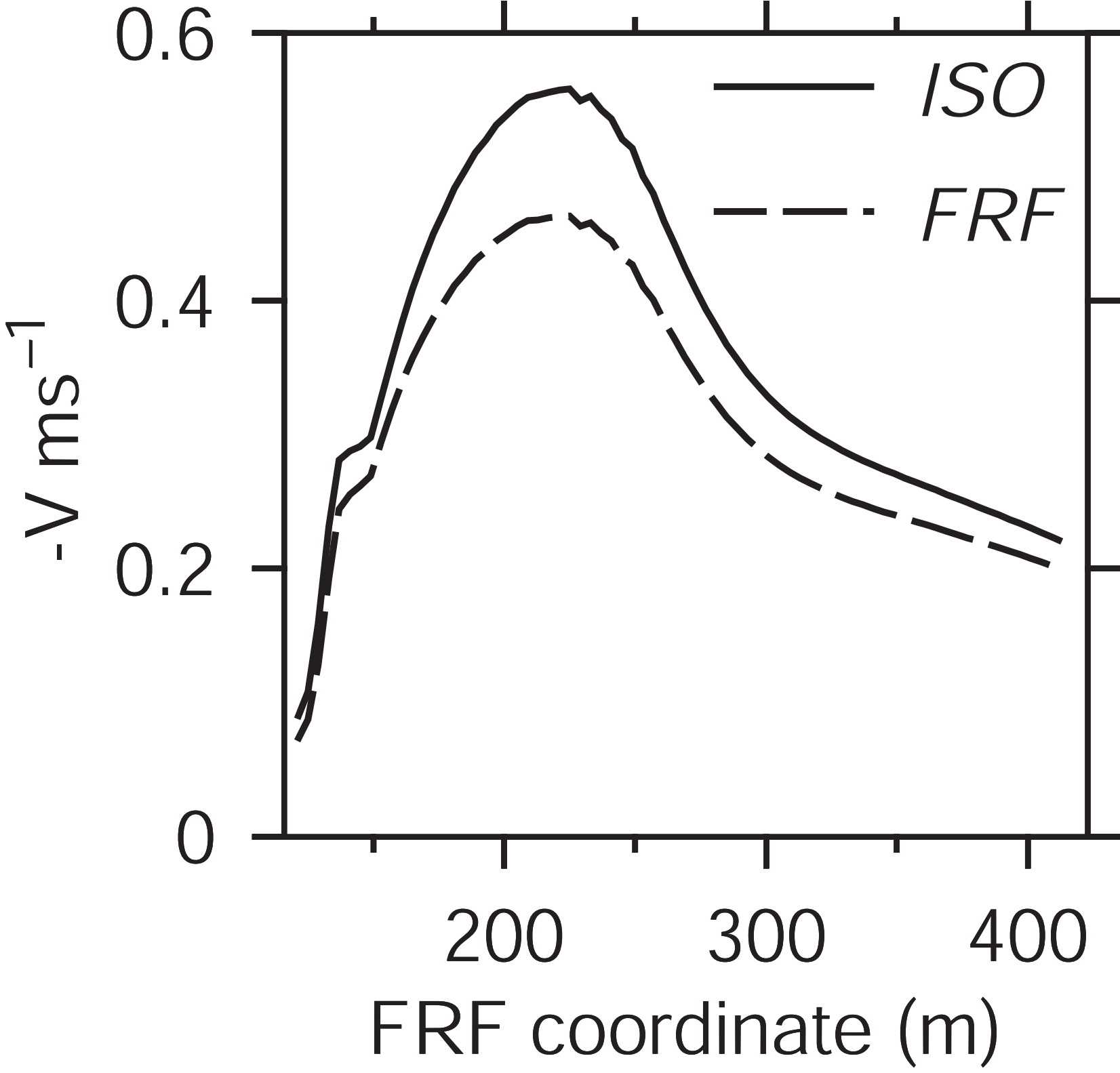
0.6
0.4
0.2
0
-V ms^{-1}
ISO
FRF
200
300
400
FRF coordinate (m)

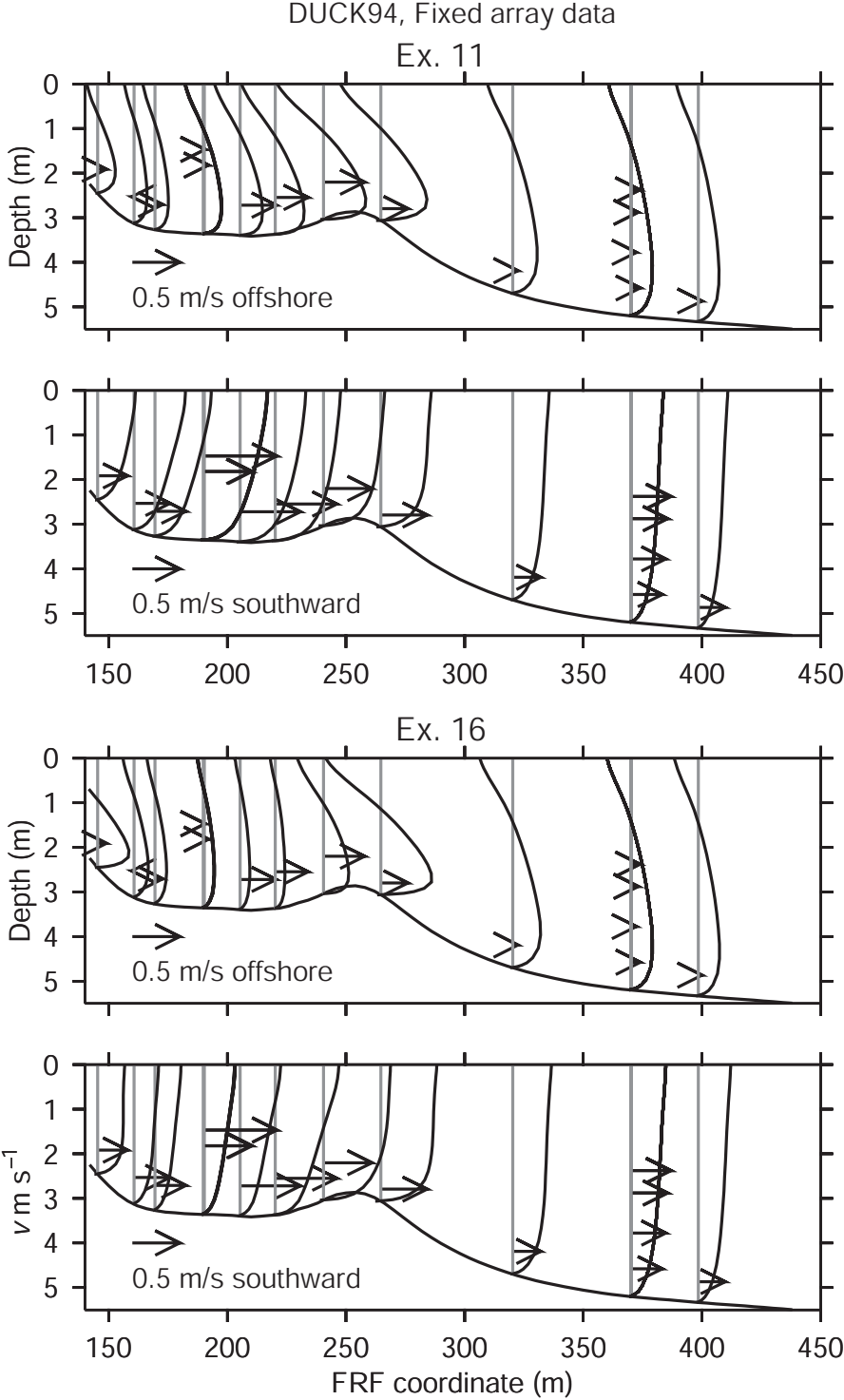
DUCK94, Fixed array data
Ex. 11
Depth (m)
0.5 m/s offshore
0.5 m/s southward
Ex. 16
Depth (m)
0.5 m/s offshore
v m s−1
0.5 m/s southward
150
200
250
300
350
400
450
FRF coordinate (m)

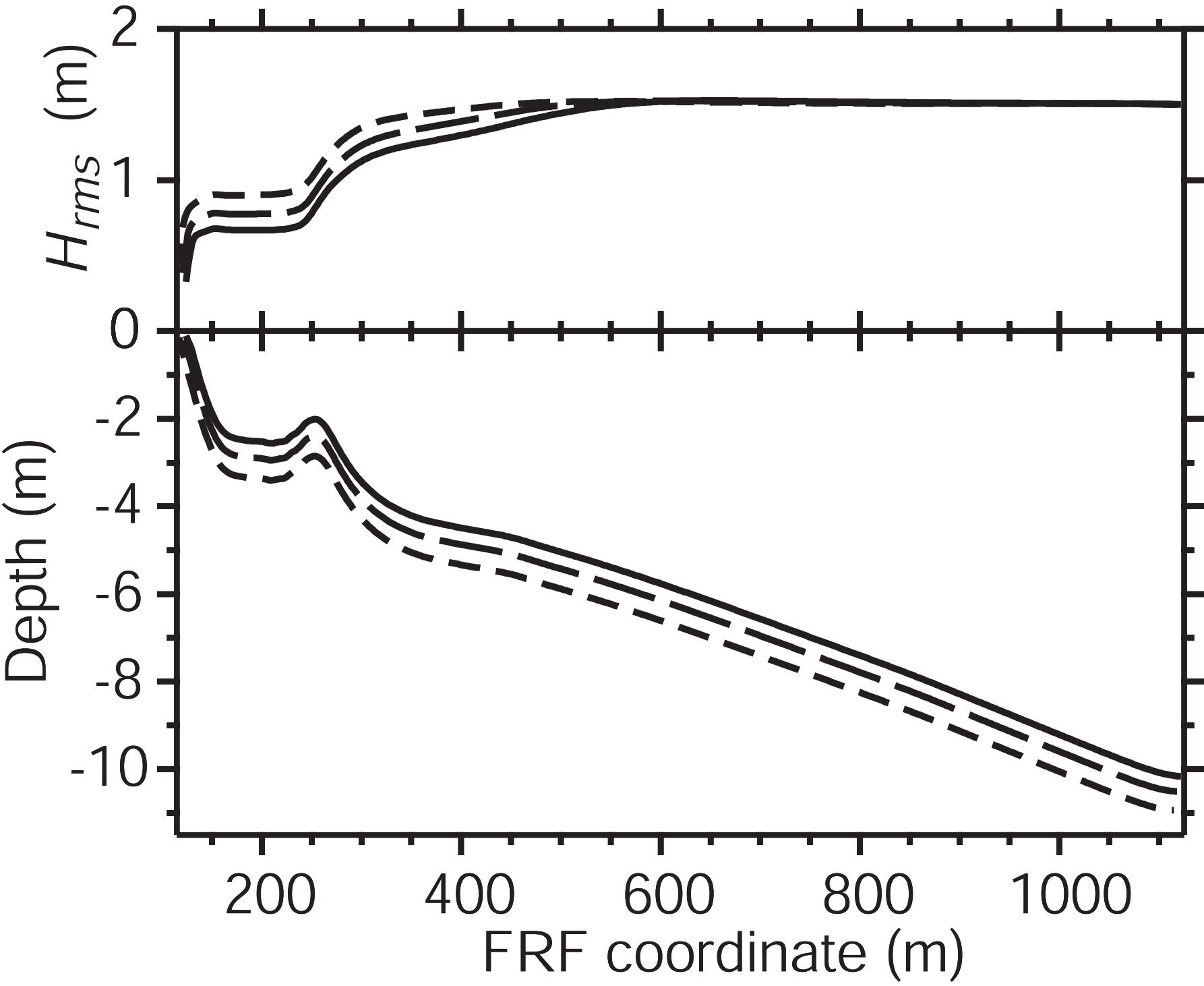
H_{rms} (m)
2
1
0
Depth (m)
-2
-4
-6
-8
-10
200
400
600
800
1000
FRF coordinate (m)

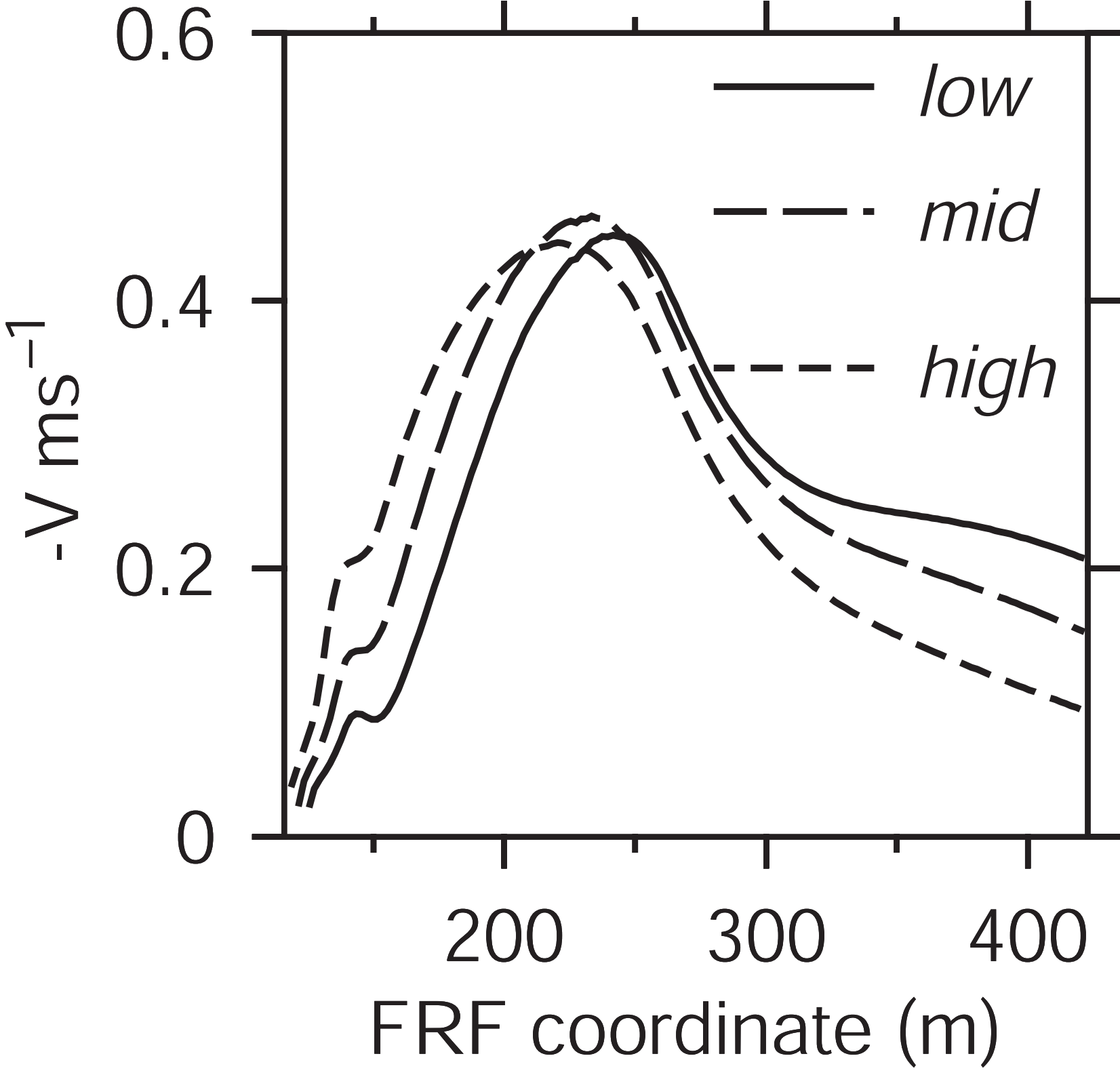
0.6
0.4
0.2
0
-V ms^{-1}
low
mid
high
200
300
400
FRF coordinate (m)

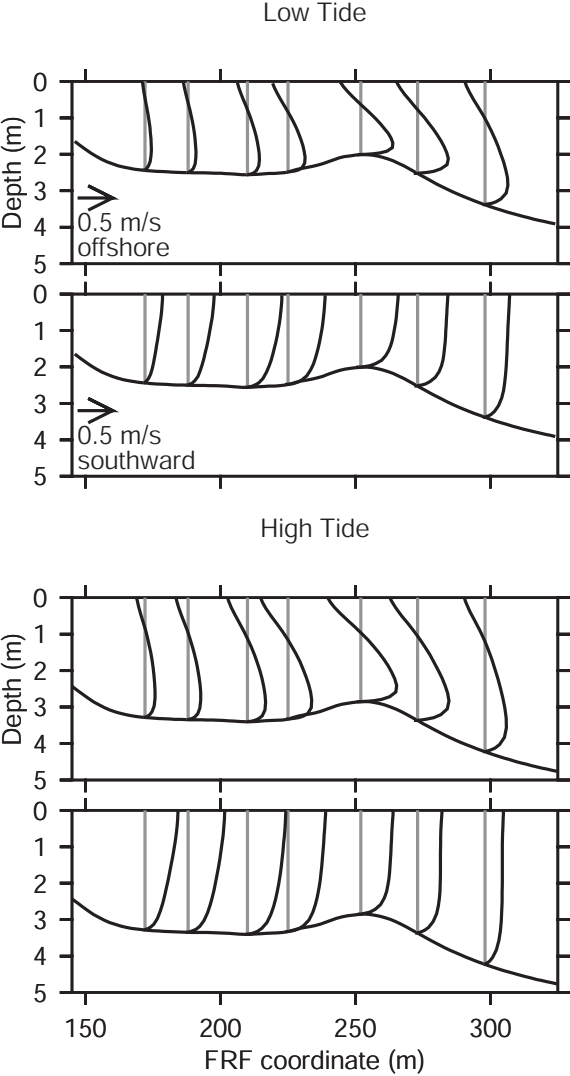
Low Tide
Depth (m)
0
1
2
3
4
5
0.5 m/s
offshore
0.5 m/s
southward
High Tide
150
200
250
300
FRF coordinate (m)

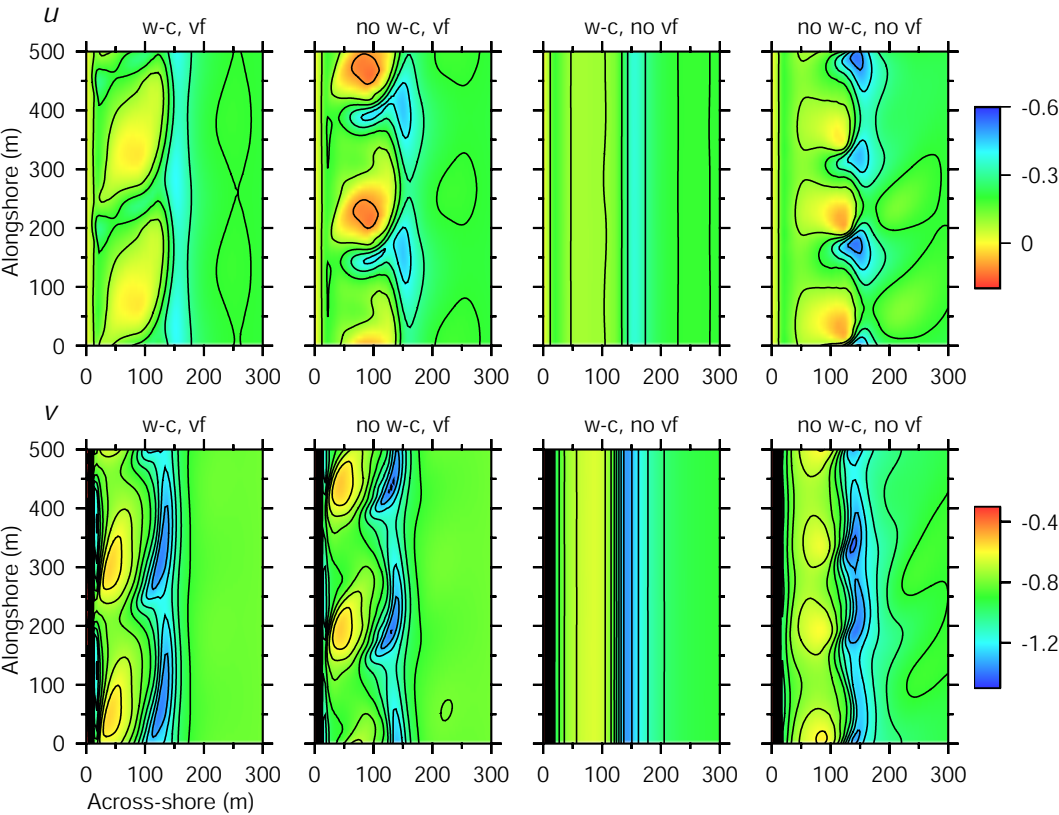
u
w-c, vf
no w-c, vf
w-c, no vf
no w-c, no vf
Alongshore (m)
0
100
200
300
400
500
-0.6
-0.3
0
v
w-c, vf
no w-c, vf
w-c, no vf
no w-c, no vf
Alongshore (m)
-0.4
-0.8
-1.2
Across-shore (m)

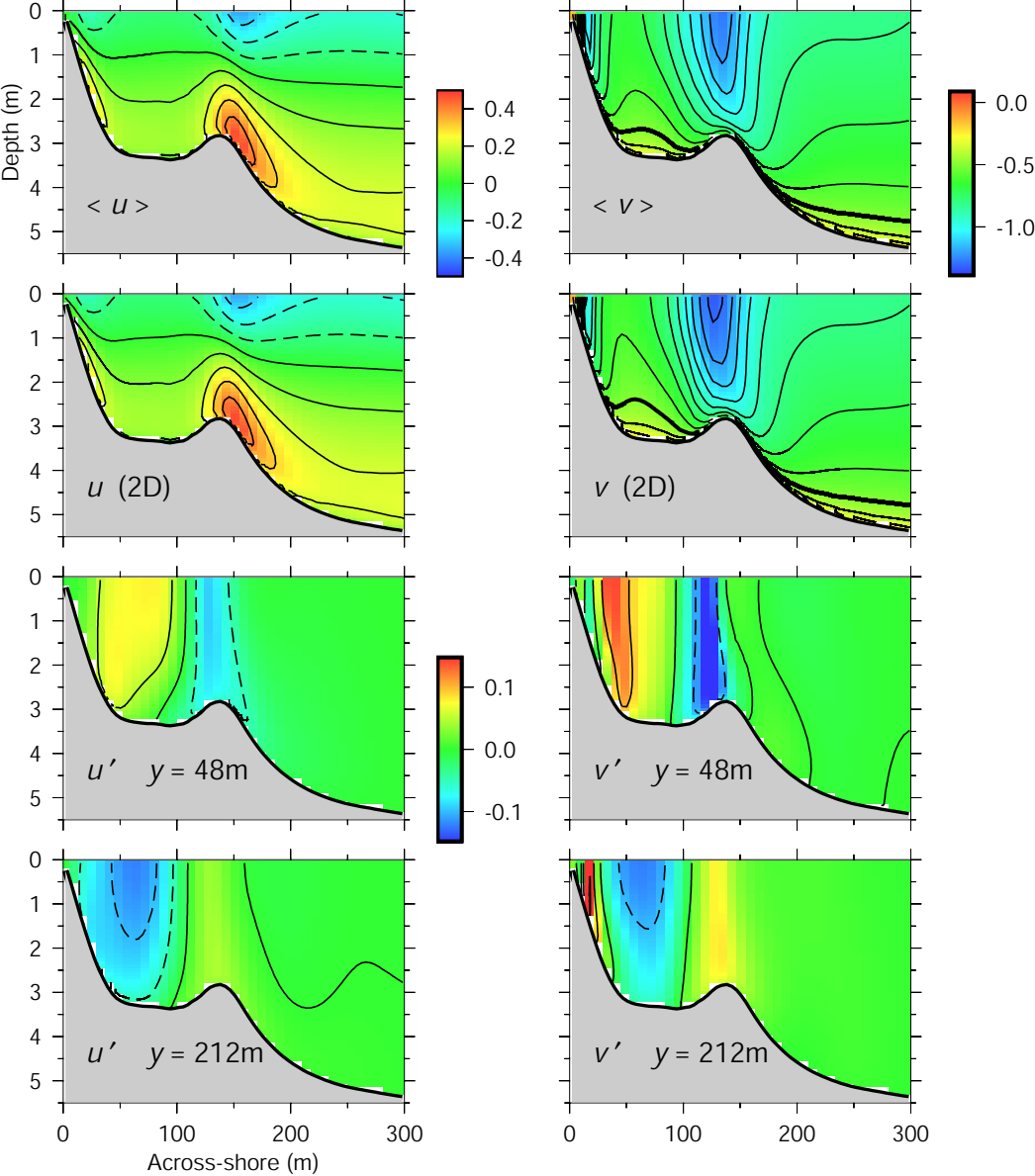
Depth (m)
0
1
2
3
4
5
< u >
0.4
0.2
0
-0.2
-0.4
< v >
0.0
-0.5
-1.0
u (2D)
v (2D)
u′ y = 48m
v′ y = 48m
0.1
0.0
-0.1
u′ y = 212m
v′ y = 212m
0
100
200
300
Across-shore (m)

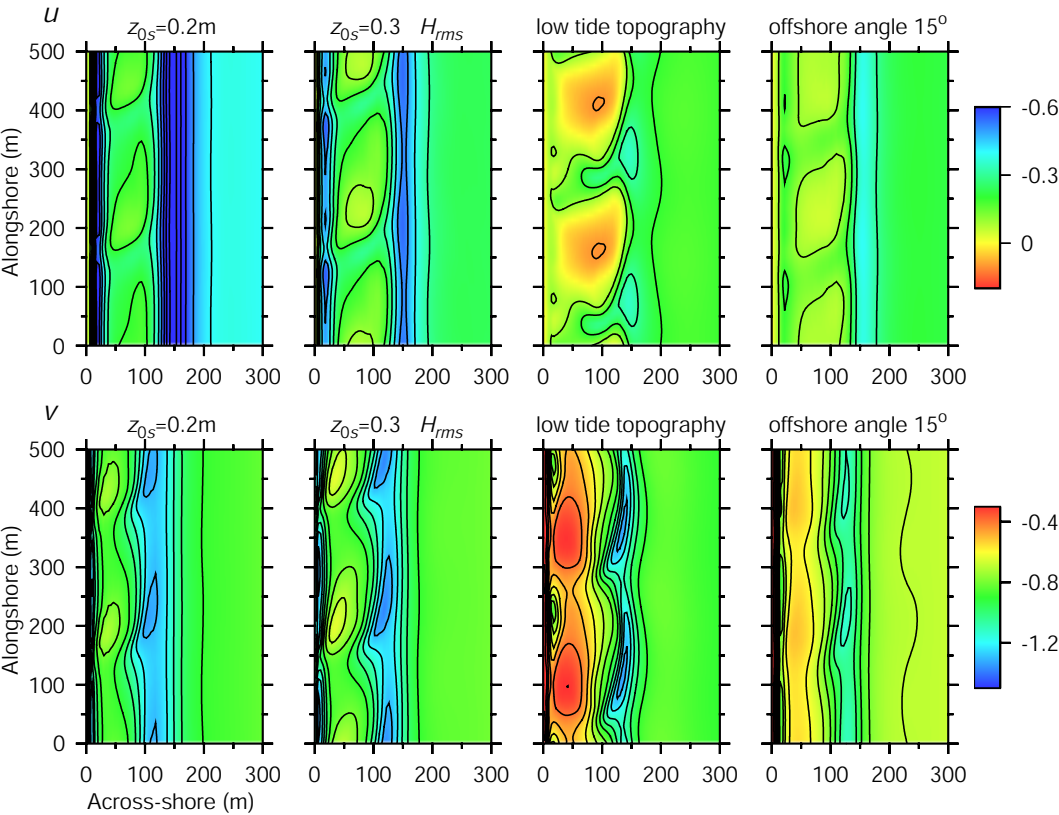
u
z_{0s}=0.2m
z_{0s}=0.3 H_{rms}
low tide topography
offshore angle 15°
-0.6
-0.3
0
v
z_{0s}=0.2m
z_{0s}=0.3 H_{rms}
low tide topography
offshore angle 15°
-0.4
-0.8
-1.2
Alongshore (m)
Across-shore (m)
0
100
200
300
400
500